Modelling the reflective cracking features of asphalt overlay for airport runway under temperature and airplane load coupling factors

Yang, Ruochong; Zhan, Chong; Sun, Long; Shi, Chenguang; Fan, Yulou; Wu, You; Yang, Jun; Liu, Hongbo

DOI
10.1016/j.conbuildmat.2024.138774

Publication date
2024

Document Version
Final published version

Published in
Construction and Building Materials

Citation (APA)
Yang, R., Zhan, C., Sun, L., Shi, C., Fan, Y., Wu, Y., Yang, J., & Liu, H. (2024). Modelling the reflective cracking features of asphalt overlay for airport runway under temperature and airplane load coupling factors. *Construction and Building Materials*, *451*, Article 138774. https://doi.org/10.1016/j.conbuildmat.2024.138774

Construction and Building Materials 451 (2024) 138774

Contents lists available at ScienceDirect

Construction and Building Materials

journal homepage: www.elsevier.com/locate/conbuildmat

Modelling the reflective cracking features of asphalt overlay for airport runway under temperature and airplane load coupling factors

Ruochong Yang [a], Chong Zhan [a], Long Sun [a], Chenguang Shi [b], Yulou Fan [a], You Wu [c,*], Jun Yang [a], Hongbo Liu [a]

[a] School of Transportation, Southeast University, #2 Southeast University Road, Nanjing 211189, China
[b] National & Local Joint Engineering Research Center of Transportation Civil Engineering Materials, Chongqing Jiaotong University, Chongqing 400074, China
[c] Faculty of Civil Engineering and Geosciences, Delft University of Technology, Stevinweg 1, Delft 2628 CN, the Netherlands

ARTICLE INFO

Keywords:
Airport runway
Asphalt overlay
Temperature-load coupling analysis
Reflective crack
Extended finite element method

ABSTRACT

Asphalt overlays have been widely employed in airport runway maintenance in recent years due to their ability to minimize traffic disruption. However, they continue to face the challenge of reflective cracks originating from the expansion joints of the underlying cement concrete runway. To better understand the cracking behavior of asphalt overlays under the combined temperature variations and aircraft loads, this study developed a finite element (FE) model. with the model incorporate two types of landing methods and typical temperature conditions. Simulation results indicate that critical loading positions are located at the edges of original cement concrete slabs, where shear stress is identified as the primary driver of crack evolution, with the peak stress coinciding with the arrival of aircraft load. Furthermore, findings suggest that the use of asphalt overlays significantly reduces the stress intensity in crack-prone areas, particularly under rough landing conditions. Reflective cracks predominantly manifest as type II shear cracks, While aircraft loading and initial crack length exert a relatively limited impact on crack propagation compared to temperature effects, the horizontal location of the initial crack substantially influences both the direction and speed of crack propagation. To mitigate crack propagation, increasing the linear shrinkage coefficient of the overlay material and the thickness of the asphalt overlay are effective strategies for enhancing the cracking resistance of airport runways with asphalt overlays. The methodologies and findings of this study provide valuable insights for engineering practices involving similar structural configurations and materials.

1. Introduction

In recent years, the significant increase in aircraft traffic and loads has heightened the demand for high-quality airport infrastructures, particularly in rapidly developing countries and regions. Taking China as a case study, the country recorded a substantial volume of 9.66 billion passengers and 46.4 billion tons of cargo in 2022, with these figures expected to continue rising rapidly in the coming years [1]. Unlike developed regions such as Europe and North America, whose asphalt airport runway percentage reach up to 62.4 % [2], nearly 90 % of Chinese airport runway applies cement concrete. This preference for cement concrete is primarily due to technological and economic considerations during the extensive constructing period. While cement concrete offers advantages such as high strength and load-bearing capacity, the increased aircraft volume and load have led to structural deterioration of airport runways. Common issues include runway separation and fracture in cement concrete slabs, posing serious threats to both the safety and longevity of airport runway [3,4]. These challenges are not unique to China but are also observed in other developing countries and regions [3,5]. Consequently, there is an urgent demand of maintaining existing airport runway in terms of improve the service level of airport.

To address these challenges, geosynthetics such as geogrids and geonets has been introduced to enhance the performance, such as moisture ability and water management, of airport runway and roadway pavement [6–8]. Despite their benefits, integrating geosynthetics with asphalt layers to improve the cracking resistance of airport runway may sometimes result in inadequate shear strength between the layers, failing to meet the requirements in some occasions [3,9,10]. Given the advantages of asphalt concrete pavement, which include a smooth, joint-free, mechanized construction, and controllable quality, the use of

---

* Corresponding author.
E-mail address: You.Wu@tudelft.nl (Y. Wu).

https://doi.org/10.1016/j.conbuildmat.2024.138774
Received 5 June 2024; Received in revised form 13 October 2024; Accepted 14 October 2024

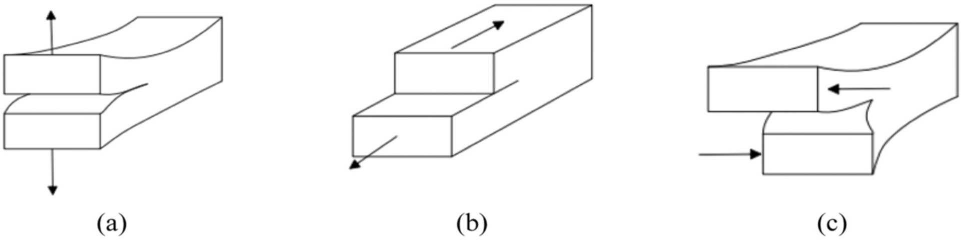

Fig. 1. Three types of cracks (a) opening mode, (b) Sliding mode, and (c) tearing mode.

asphalt concrete exclusively for airport pavement maintenance – known as the asphalt overlay – presents a viable alternative [11,12]. This method has been widely adopted for runway maintenance especially in developing countries and regions. Nonetheless, long-term usage of asphalt overlay still encounters significant issues, such as cracking and rutting. Cracking is primarily induced by the heavy aircraft load, while rutting is caused by temperature fluctuations. Notably, reflective cracking within the internal structure poses a substantial threat to the safety and comfort of airport runways, as its propagation is challenging to monitor and assess both in field conditions and laboratory settings [13–15].

The presence of joints and other cracks in the original concrete slab compromises the integrity of any added asphalt overlay, as these defects propagate under aircraft load and temperature variations [15–18]. Similar issues are observed in pavement engineering, which has been extensively studied both through laboratory tests and numerical simulations. As a result, general theories and testing methods have been developed and applied during the process [5,19–22], making it easier to investigate the phenomenon in airport runway. Typically, fracture mechanics and finite element (FE) method are the most effective approaches for studying reflective cracks in both pavement engineering and airport runway [11,23,24]. For instance, Lytton [25] examined differences between cracked pavement and uncracked pavement using fracture mechanics, detailing the propagation of reflective cracks within pavement structure. Kuai [26] further explored the impact of temperature and void ratio of asphalt mixture on the cracking behavior of pavement structures using J-integral, thereby predicting the lifespan of pavement structures with asphalt overlays. In the context of airport runways, Qian [27] proposed a composite airport runway structure with enhanced rutting resistance, comprising an epoxy asphalt layer, a stone mastic asphalt (SMA) layer and an asphalt concrete (AC) layer. Liu [28] developed a 3D FE model for airport runways with an epoxy asphalt overlay, and studied the effects of overlay thickness and modulus. Ran [29,30] compared the performance of SMA and epoxy asphalt in airport runways using Superpave design method, demonstrating superior rutting resistance for epoxy asphalt.

However, these studies primarily focus on single performance of airport runways under high-temperature conditions, emphasizing rutting resistance while often neglecting the issue of reflective cracking in asphalt overlays. Moreover, limited availability of application sites makes it difficult to monitor the cracking behavior of runway asphalt overlays under varying conditions, highlighting the need for more practicable methods, such as numerical simulations. While semi-analytical methods have been widely used in both pavement and airport runway analyses [31], their complexity makes it challenging to evaluate cracking behavior of airport runways with initial cracks. In contrast, the FE method simplifies the modelling process, and its combination with fracture mechanics has proven effective for describing the cracking behavior of structure [32–34]. Despite its advantages, research on the cracking behavior of airport runways with asphalt overlays remains limited, primarily due to the lack of extensive engineering practice. Additionally, early versions of popular FE software such as ABAQUS and ANSYS had limited capabilities in simulating cracking behavior under load-temperature coupling conditions, further hindering the development of runway asphalt overlay analysis. Recent advancements in computational technology have made it feasible to analyze the cracking behavior of asphalt overlays before practical implementation [17,21,35].

The primary challenges concerning the cracking behavior of airport runway asphalt overlay involve rutting and cracking under load-temperature coupling conditions. Although the application of thermosetting asphalt mixtures as significantly improved rutting resistance [27,28], cracking remains a critical issue that affects the long-term safety and comfort of airport runways. To thoroughly investigate the cracking behavior of airport runways with asphalt overlays under varying temperature-load coupling conditions, this study develops a corresponding runway model and analyzes the development of reflective cracks under different scenarios. The findings aim to provide valuable insights for engineering practice. This paper was organized as follows:

Firstly, the fundamental theories and methodology employed in this study are introduced, with a particular focus on the extended finite element method (XFEM) and temperature field approach. Then, a typical airport runway model with asphalt overlay, subject to various temperature-load conditions and initial cracks, is established. Next, the cracking features of the airport runway, including the critical loading positions and stress intensity factors, are analyzed based on the model. Subsequently, different factors influencing the cracking behavior of airport runway under diverse load and temperature conditions are discussed in detail. Finally, the main findings and conclusions are detailed in the last section.

2. Methodology

In this study, the cracking behavior was primarily analyzed using fracture mechanics, with related parameters including the stress intensity factor [23,32], and energy release rates [36,37]. Besides, the XFEM was implemented in the FE software ABAQUS to simulate the propagation of reflective crack [24,38,39]. During the temperature-load coupling analysis, the periodic solar radiation was applied [40]. The basic theories mentioned above were detailed elsewhere and this section mainly focused on the most pertinent theories that were used.

2.1. Basic theory of fracture mechanics

According to fracture mechanics, cracks are divided into three types: Type I, Type II and Type III, which are referred to as opening mode, sliding mode and tearing mode, respectively, as shown in Fig. 1. In Type I cracks, the tensile stress in the crack region is perpendicular to the cracking surface. In Type II cracks, the tensile stress is parallel to both the cracking surface and crack tip line. In contrast, for type III cracks, the stress is oriented longitudinally, perpendicular to the side of cracking region. Based on previous researches [4,18,41], the primary crack types in the airport runway with asphalt overlays are Type I, Type II and mixed Type I + Type II, which are similar to those the cement concrete pavements with asphalt overlays.

For all three types, their corresponding stress intensity factors, denoted K_I, K_{II} and K_{III}, are defined through Eq. (1)~(3):

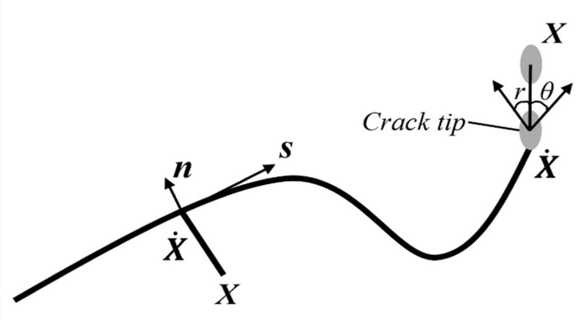

Fig. 2. Additional functions at crack tip.

$$K_I = \lim_{r\to 0}\sqrt{2\pi r}\sigma_y(r,0)\# \tag{1}$$

$$K_{II} = \lim_{r\to 0}\sqrt{2\pi r}\tau_{xy}(r,0)\# \tag{2}$$

$$K_{III} = \lim_{r\to 0}\sqrt{2\pi r}\tau_{yz}(r,0)\# \tag{3}$$

where σ_y and τ_{xy} are stress components at the crack tip, which can be calculated using equations introduced elsewhere [16].

By applying the stress intensity factor, the trend of cracking propagation can be effectively determined using the K principle. For instance, in case of Type I crack, the critical K value under plane stress and plane strain conditions is denoted as K_i and K_{iC}, respectively. If the stress intensity factor $K \geq K_i$ or $K \geq K_{iC}$, the crack at this location is likely to propagate. A similar criterion can be applied to other two types of cracks or mixed type cracks.

Specifically, for airport runway with asphalt overlays, the mixed Type I + Type II also occur within the structure. Under these conditions, the rotation angle φ and twisting angle ψ can be calculated using Eq. (4) and Eq. (5), respectively:

$$K_I\sin\varphi + K_{II}(3\cos\varphi - 1) = 0\# \tag{4}$$

$$\tan 2\psi = \frac{2K_{III}}{K_{eff-1,2}(1-2\nu)}\# \tag{5}$$

where $K_{eff-1,2}$ is the effective stress intensity factor for a mixed Type I + Type II crack, which can be calculated using Eq. (6):

$$K_{eff-1,2} = \frac{0.83K_I + \sqrt{0.45K_I^2 + 3K_{II}^2}}{1.5}\# \tag{6}$$

Additionally, the cracking behavior can be described using energy release rate, known as the G principle [36]. According to this theory, for a two-dimensional crack, the energy release rate G can be calculated using crack closure integral, as shown in Eq. (7):

$$G = \lim_{\Delta a\to 0}\frac{1}{\Delta a}\int_0^{\Delta a}\sigma_{i2}(x_1,0)u_i(\Delta a - x_1,\pi)\mathrm{d}x_1\# \tag{4}$$

where Δa is the new crack length, and the displacement components are written as functions of the polar coordinates $r = \Delta a - x_1$ and $\theta = \pi$.

2.2. XFEM method

To describe the crack length, the XFEM is widely applied in FE software. Based on the partition of unit theory [42,43], XFEM posits that any function $\varphi(x)$ can be decomposed into local functions $N_i(x)\varphi(x)$, as shown in Eq. (8):

$$\varphi(x) = \sum_{i=1}^{n}N_i(x)\varphi(x), \sum_{i=1}^{n}N_i(x) = 1\# \tag{8}$$

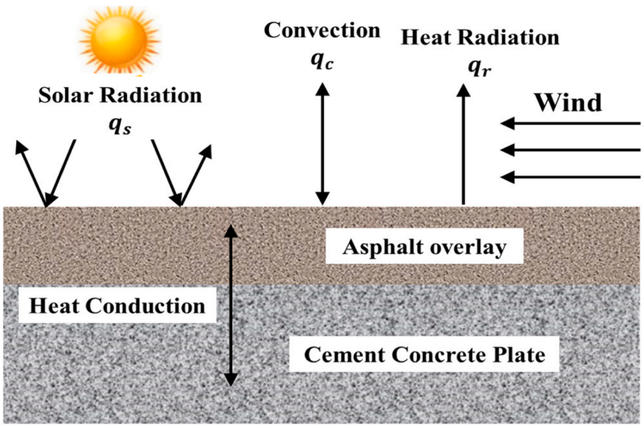

Fig. 3. Schematic of calculating temperature field.

when the cracks propagate, a crack tip asymptotic function is added to approximate the jump function, reflecting the surface discontinuity of the crack, as depicted in Fig. 2. Additionally, extra degrees of freedom are introduced to describe the displacement discontinuity of the crack, as shown in Eq. (9):

$$u = \sum_{i=1}^{n}N_i(x)\left[u_i + H(x)a_i + \sum_{\alpha=1}^{4}F_\alpha(x)b_i^\alpha\right]\# \tag{9}$$

where u represents displacement vector of any point in the region. u_i represents the normal displacement vector of a typical point. $N_i(x)$ are the shape functions of any point in the region. a_i represents the vector associated with intermittent additional degrees of freedom. b_i^α denotes the vector corresponding to singularity additional degrees of freedom. $F_\alpha(x)$ is a function that reflects the singularity at crack tip. $H(x)$ is a jump function that captures the surface discontinuity at crack tip.

When applying XFEM in calculating crack growth, only the maximum principle criterion can achieve the free growth of a crack in FE software. This principle is described by Eq. (10):

$$f = \left\{\frac{\langle\sigma_{\max}\rangle}{\sigma_{\max}^0}\right\}\# \tag{10}$$

where $\sigma_{\max}$ and $\sigma_{\max}^0$ represent the maximum principle stress and maximum allowable stress, respectively. Besides, the method for evaluating and describing crack evolution is introduced in Ref. [44].

2.3. Temperature field and convection heat transfer

During the operation of airport runways, aircraft load and temperature are two main factors influencing the internal stress of the structure. Furthermore, the relationship between temperature and thermal stress is weakly coupled, meaning that temperature variations significantly impact stress, but stress variations have limited influence on temperature field. Based on this characterization, thermal-force sequential coupling analysis was applied in this study [40,45]. The analysis process can be divided into two steps: the first step involves calculating the temperature field, and the second step involves calculating the stress field by applying the temperature field as a volumetric load.

In determining the temperature field, the primary heat source for the airport runway is short-wave radiation originating from the sun, which can be simplified to heat flux. Meanwhile, the radiation of airport runway is assumed to occur through convection. The entire solar radiation and convection process is illustrated in Fig. 3.

During the process, the heat flux q consists of three components: solar radiation q_s, convection heat transfer q_c, and effective surface heat radiation q_r. Thus, q can be calculated using Eq. (11).

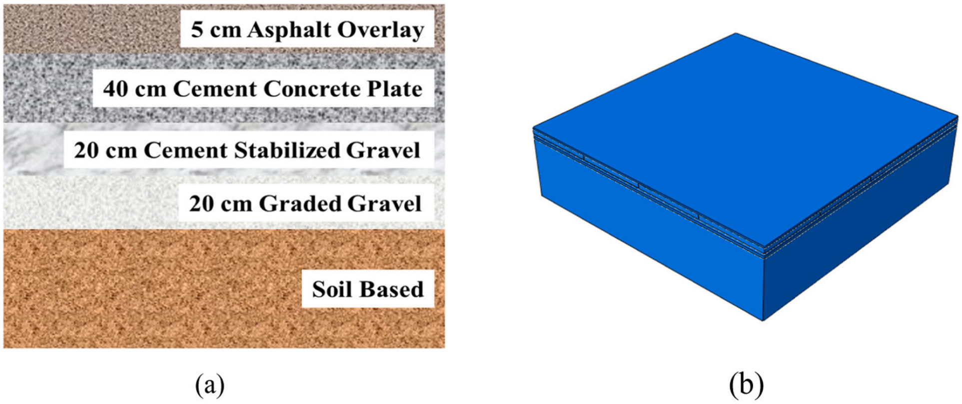

Fig. 4. Schematic of typical airport runway with asphalt overlay (a) structure, and (b) FE model.

$$q = q_s + q_c + q_r \# \tag{11}$$

The three components can be calculated separately. For solar radiation q_s, its variation intensity on a sunny day can be approximated using a sine or cosine function, as shown in Eq. (12)[46,47].

$$q_s(t) = \begin{cases} 0, \quad 0 \le t \le 12 - \dfrac{c}{2} \\ q_0 \cos m\omega(t-12), \quad 12 - \dfrac{c}{2} < t \le 12 + \dfrac{c}{2} \\ 0, \quad 12 + \dfrac{c}{2} < t \le 24 \end{cases} \# \tag{11}$$

where q_0 is the maximum daily solar radiation (J/m^2),calculated as $q_0 = 0.131mQ, m = 12/c$. Here, c is the effective daylight hours, Q is the total daily radiation, and ω is the frequency with a value of $\pi/12$.

However, since the above function is a non-smooth continuous function with jump discontinuities, it is necessary to represent it using a smooth continuous series, such as Fourier series, as shown in Eq. (12). Engineering practice indicates that when the order $k = 30$, the accuracy of this equation can meets the requirements.

$$q_s(t) = \frac{a_0}{2} + \sum_{k=1}^{\infty} a_k \cos \frac{k\pi(t-12)}{12} \# \tag{12}$$

where $a_0 = \frac{2q_0}{m\pi}$ and a_k can be calculated using Eq. (13).

$$a_k = \begin{cases} \dfrac{q_0}{\pi}\left[\dfrac{1}{m+k}\sin(m+k)\dfrac{\pi}{2m} + \dfrac{\pi}{2m}\right], \quad k = m \\ \dfrac{q_0}{\pi}\left[\dfrac{1}{m+k}\sin(m+k)\dfrac{\pi}{2m} + \dfrac{1}{(m-k)}\sin(m-k)\dfrac{\pi}{2m}\right], k \ne m \end{cases} \# \tag{13}$$

The user subroutines (DFLUX) was applied in ABAQUS to define the absorbed amount of solar radiation.

For the second component of heat flux, the convection heat transfer can be calculated using Eq. (14)[48].

$$q_c(t) = a_c[T_a(t) - T_s(t)] \# \tag{14}$$

where a_c is the convective heat transfer coefficient. $T_a(t)$ is the ambient temperature around the asphalt overlay, and $T_s(t)$ is the temperature at the surface of the asphalt overlay. The convective heat transfer coefficient a_c is usually related to the wind speed on the surface of asphalt overlay v_w and can be calculated using Eq. (15).

$$a_c = 3.7v_w + 9.4 \# \tag{15}$$

Additionally, the daily ambient temperature $T_a(t)$ can be calculated using Eq. (16).

$$T_a(t) = \overline{T_a} + T_m[0.96\sin\omega(t-t_0) + 0.14\sin 2\omega(t-t_0)] \# \tag{16}$$

where $\overline{T_a}$ is the average temperature of the monitored day. T_m is the difference between the highest and lowest temperature in a day, and t_0 is initial phase. The user subroutine (FILM) was applied in ABAQUS to model the convective heat transfer behavior.

For the third component, the effective surface heat radiation q_r, it can be calculated using Eq. (17)[49].

$$q_r = \varepsilon\sigma\left[\left(T_1|_{Z=0} - T_Z\right)^4 - \left(T_a - T_Z\right)^4\right] \# \tag{17}$$

where ε is the surface emissivity, valued at 0.81 for asphalt overlay. σ is the Stefan-Boltzman constant, valued at 5.6697×10^{-8}. $T_1|_{Z=0}$ is the temperature at the overlay surface. T_a is the ambient temperature. T_Z is the absolute zero temperature, valued at -273 °C.

3. Modelling the airport runway with asphalt overlay

3.1. Geometric model

In this study, a typical airport with an asphalt overlay was selected as the example to characterize the cracking features of overlay structure, as illustrated in Fig. 4(a). The original airport runway consists of four layers: a cement concrete layer with a thickness of 40 cm, a cement stabilized gravel with a thickness of 20 cm, a graded gravel with a

Table 1
Material parameters of the structure [40,52].

Layer	Density /(kg·m^{-3})	Elastics modulus /MPa	Poisson's ratio	Expanding coefficient /°C^{-1}	Thermal capacity /(J·m^{-1}·h^{-1}·°C^{-1})	Thermal conductivity /(J·kg^{-1}·°C^{-1})
Overlay	2500		0.25	2.6×10^{-5}	925	4660
Cement Concrete Plate	2800	34400	0.15	1.2×10^{-5}	902	5626
Cement Stabilized Gravel	2200	1700	0.25	6×10^{-6}	960	5616
Graded Gravel	2300	1600	0.25	6×10^{-6}	960	5616
Soil Base	1800	80	0.4	4.5×10^{-6}	901	2160
Steel Rods	7850	210000	0.3	1.35×10^{-5}	465	161954

thickness of 20 cm, and a soil base. To avoid the negative influence of boundaries, the thickness of soil base layer in the model is set to 5 m. Additionally, the thickness of asphalt overlay is set to 5 cm. Regarding the runway structure, all layers except for the cement concrete layers are continuous. The cement concrete layer is composed by runway slabs, each measuring $5m \times 5m$. The width of the joints between the slabs is set to 8 mm. There are a total of 16 slabs in the model, arranged in 4×4 grid. Consequently, the overall dimensions of the model are $20.024m \times 20.024m \times 5.85m$. During the calculating process, the boundary condition in the vertical direction (the load direction) was fixed. The boundary conditions in the longitudinal and horizontal directions were set as zero displacement in the X Y directions, respectively.

During the analysis, all materials were treated as homogeneous linear elastic materials, and their basic material properties, including thermal parameters, are uniformly listed in Table 1. It is important to note that the fracture energy obtained through indoor semi-circular bending (SCB) tests was used as the critical material parameter to control cracking behavior. The validity of this approach has been confirmed in previous research [32]. This study examines two types of asphalt mixtures used in airport runway overlays: SMA-13 and EAM-13. According to the methodology described in Ref. [32], the fracture energy values for these materials were determined using indoor SCB tests. The fracture energy for SMA-13 and EAM-13 are 383.76 J/m^2 [50] and 1706.42 J/m^2 [51], respectively. Other thermal-related parameters and densities are set identically for both mixtures, as they are asphalt-based materials with similar aggregate grading, as shown in Table 1. Additionally, the viscoelastic properties of SMA-13 and EAM-13 are described using the generalized Maxwell model. In ABAQUS, this is implemented via an 11-order Prony series, whose accuracy has been validated by previous research [32,34]. Specific values for SMA-13 and EAM-13 are referenced from Ref. [34] and are not detailed here for the sake of brevity. In Table 1, the elastic modulus of the overlay is not listed since a viscoelastic constitutive model was employed. The wind speed v_w was set to 2.9 m·s^{-1} based on the meteorological data. Moreover, both the steel transmission bar and tie rod at the joint have a diameter of 0.038 m and a length of 0.55 m.

3.2. Load of aircraft

Two types of aircraft loads were considered in this study: sliding load and rough landing, to simulate different working conditions of the asphalt overlay. The sliding load F_s is mainly composed of two components, those are, the static load F_I and the dynamic load F_{II}, represented as:

$$F_s = F_I + F_{II}\# \tag{18}$$

where F_I and F_{II} can be calculated using Eq. (19) and Eq. (20), respectively.

$$F_I = \frac{G_s}{N}\left(1 + K_p - K_c\right)\# \tag{19}$$

$$F_{II} = \frac{G_s}{N}(K_c - 1)\sin\omega t\# \tag{20}$$

where G_s is a single axle load of the landing gear. K_p and K_c are dynamic coefficients, and N is the number of wheels. Based on previous research [53], K_p can be calculated using Eq. (21).

$$K_p = 1 + 0.023\sqrt{v} - 0.00015031v^2\# \tag{21}$$

when $v = 11.31m/s$, the maximum value of K_p is 1.058, and corresponding K_c is 1.077. Therefore, the sliding load F_s can be expressed as

$$F_s = 222.988 + 17.586\sin(18.175t)\# \tag{22}$$

For the rough landing load, it is generally accepted that an aircraft will bounce several times when landing on the airport runway at a high speed. According to Liu's research [54], the load of landing process of Boeing 747 aircraft can be depicted as shown in Fig. 5.

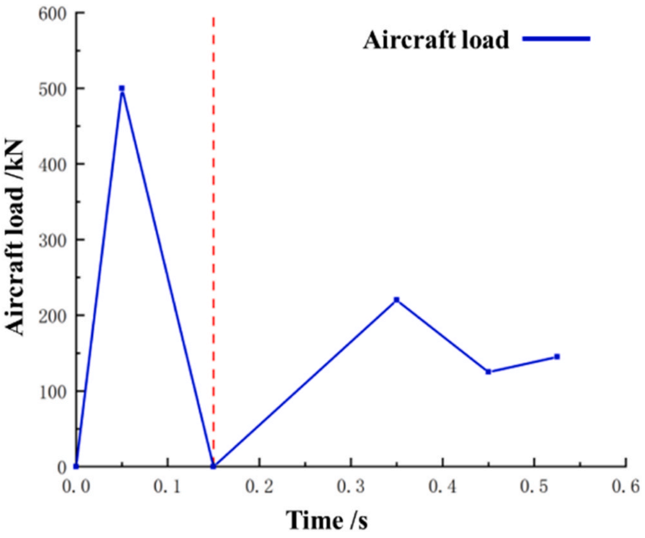

Fig. 5. Schematic of rough landing aircraft load.

During the simulation, only the first jump – spanning from 0 s to 0.15 s – was considered, as the amplitude of subsequent lateral jump is much lower and has limited influence on the crack propagation. To incorporate both the sliding load and rough landing load during the simulation, the user subroutine VDLOAD in ABAQUS was utilized.

3.3. XFEM model and working condition

The FE software ABAQUS was used to perform the entire calculation. To achieve load-temperature coupling analysis, a temperature-displacement coupled step was employed in the FE model, and the corresponding three-dimensional 8-node thermo-displacement coupled element (C3D8RT) was used for meshing the entire model during temperature-load coupling analysis. For static and dynamic analyses without temperature field, the model was meshed with three-dimensional 8-node reduced integration element (C3D8R). The schematic of the meshed model is shown in Fig. 6(a).

Additionally, the XFEM was employed to handle arbitrary discontinuities without requiring mesh reconstruction. This approach allows the model to be generated based on the structural dimensions, with conventional displacement functions at the crack tip enhanced by additional functions. Consequently, a critical aspect of the modelling process was setting the initial reflective XFEM crack in the runway structure. In this study, the level set technique was used to generate the initial cracks, with its fundamental theories detailed elsewhere [55].

The initial crack was placed at the bottom of asphalt overlay, oriented with the crack surface facing vertically upward (in the positive Z-axis direction). The bottom end of the crack intersected vertically with the bottom surface of the paving overlay layer, and the crack extended horizontally, parallel to the horizontal joints, across the entire width of the asphalt overlay, as depicted in the left image of Fig. 6(b). To enhance the convergence during the calculation of the stress intensity factor, the mesh around the crack tip was manually refined, as shown in the right image of Fig. 6(b).

To ensure clarity in subsequent presentations, the working conditions analyzed in this study are outlined as follows:

Firstly, the distribution schemes for normal sliding loads and rough landing loads are shown in Fig. 7(a) and Fig. 7(b), respectively. In Fig. 7(a), the slide speed is 11.59 m/s, the slide time is 2.2 s, and the sliding distance is 25.20 m. In Fig. 7(b), the initial landing speed is 74.9 m/s, the landing duration is 0.15 s, and the sliding distance is 11.24 m. The block dots in these figures represent the contact points between the

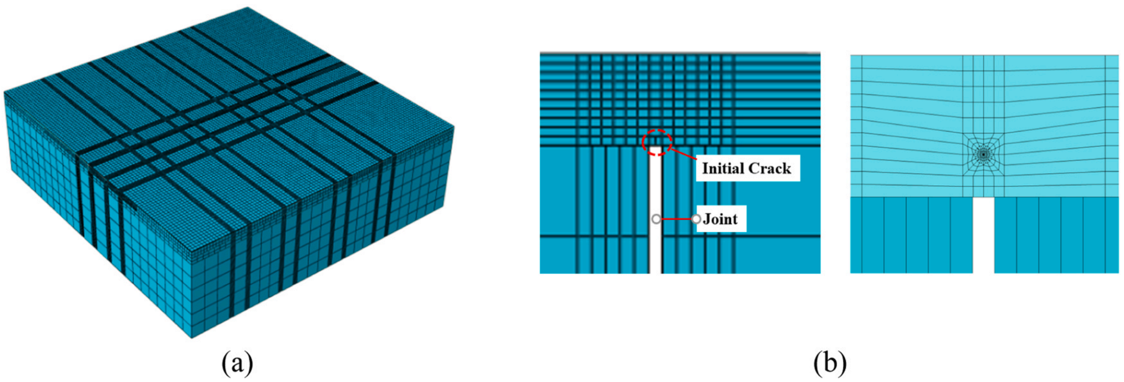

Fig. 6. Schematic of (a) meshed model, and (b) location of initial crack.

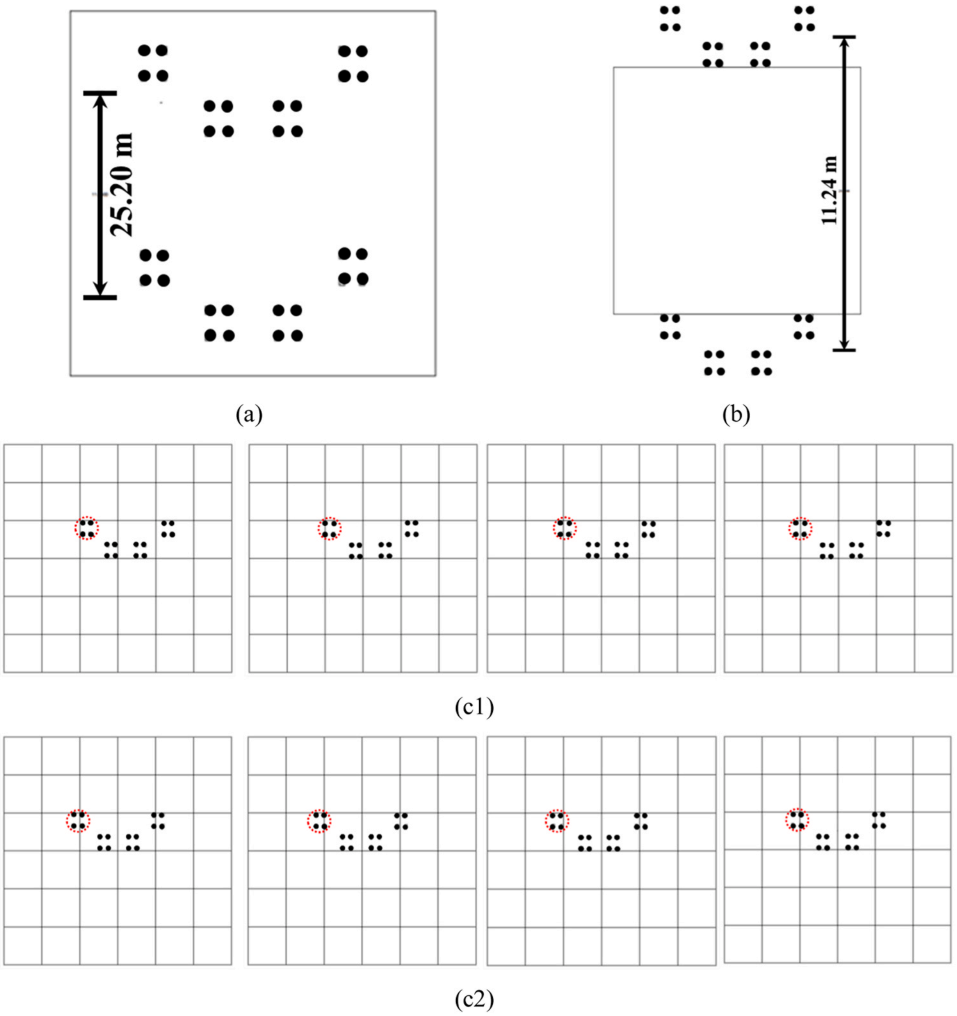

Fig. 7. Schematic of load distribution (a) sliding load, (b) rough landing load, (c1) static load position for Q8-Z1∼Q8-Z4, (c2) static load position for Q8-Z5∼Q8-Z8.

landing gear and the airport runway. Each adjacent group of four dots represents one landing gear, and the four sets of landing gears indicate the initial and final positions of the aircraft.

Secondly, to analyze the critical load positions under static load, 32 different static load distribution schemes were investigated. These 32 schemes are categorized into four types: front eight tires-longitudinal joints, front eight tires-transverse joints, back eight tires-longitudinal joints, and back eight tires-transverse joints. The categories are designated as Q8-Z1∼Q8-Z8, Q8-H1∼Q8∼H8, H8-Z1∼H8-Z8, H8-H1∼H8-H8. In each category, the number 1 denotes a load position directly adjacent to one side of the joint, while the number 8 denotes a position directly adjacent to the opposite side of the joint. For instance, the load positions categorized as Q8-Z1∼Q8-Z8 are illustrated in Fig. 7(c1) and Fig. 7(c2). This figure displays eight images depicting the relative positions between the landing gear and the airport runway joint, ranging from completely on one side of the joint to entirely on the other side. The mechanical response for each load position was analyzed to determine the critical static load position.

Table 2
Maximum absolute value of S13 under different loading conditions.

Q-Z	Max S13 (Pa)	Q-H	Max S13 (Pa)	H-Z	Max S13 (Pa)	H-H	Max S13 (Pa)
Q8Z1	1.45E+06	Q8H1	8.53E+05	H8Z1	1.33E+06	H8H1	1.23E+06
Q8Z2	1.30E+06	Q8H2	1.18E+06	H8Z2	1.31E+06	H8H2	1.27E+06
Q8Z3	1.32E+06	Q8H3	1.12E+06	H8Z3	1.31E+06	H8H3	9.21E+05
Q8Z4	1.19E+06	Q8H4	7.99E+05	H8Z4	1.50E+06	H8H4	9.74E+05
Q8Z5	1.36E+06	Q8H5	8.24E+05	H8Z5	1.42E+06	H8H5	1.45E+06
Q8Z6	1.31E+06	Q8H6	1.19E+06	H8Z6	1.30E+06	H8H6	1.42E+06
Q8Z7	1.30E+06	Q8H7	1.16E+06	H8Z7	1.55E+06	H8H7	1.36E+06
Q8Z8	1.33E+06	Q8H8	8.92E+05	H8Z8	1.31E+06	H8H8	8.79E+05

*Note: In the table and related expressions, Q8 refers to the front eight tires of main landing gears, while H8 refers to the rear tires of main landing gears. Z denotes a longitudinal joint, and the latter H denotes atransverse joint.

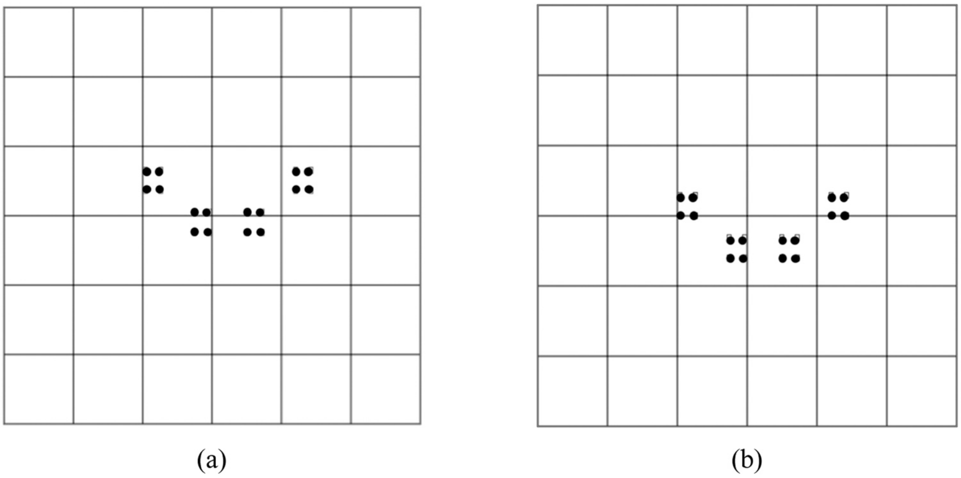

Fig. 8. Schematic of load position (a) Q8Z1H6, and (b) H8Z7H5.

4. Results and discussion

4.1. *Cracking features under static load approach*

4.1.1. *Critical load position*

To align the mechanical response of an airport runway under dynamic loads with that under static loads, a dynamic load factor is typically applied. Unlike dynamic loads, which vary the loading position over time, static loads maintain a fixed position and must be varied to approximate the dynamic response as closely as possible. Similar to cement concrete pavements with asphalt overlays, the primary effect of the load is on the shear stress at the bottom of asphalt overlay, which in turn influence the propagation of reflective cracks. Therefore, this section investigated the shear stress S13 at the bottom asphalt overlay under different load conditions, as detailed in Table 2.

Table 2 shows that the maximum shear stress S13 occurs under load conditions Q8Z1, Q8H6, H8Z7, H8H5, respectively, for each category. However, in practical scenarios, it is challenging to standardize the exact positions of all front and rear tires. Therefore, the relative positions of the transverse and longitudinal joints for the front and rear tires are combined. The mechanical response is then compared between the load configurations Q8Z1H6 andH8Z7H5.The two load distributions are illustrated in Fig. 8(a) and Fig. 8(b), respectively.

The calculation results show that the maximum shear stress S13 under load conditions Q8Z1H6 and H8Z7H5 are 1.21×10^6 Pa and 1.59×10^6 Pa, respectively. The results indicate that the maximum shear stress in H8Z7H5 is higher than that for Q8Z7 and other individual configurations. For the H8Z7H5 load condition, the maximum shear stress occurs directly above the transverse central joint, whereas for the Q8Z7 condition, it occurs above a transverse joint near the edge. The boundary conditions used in the simulation can cause stress concentrations at the model boundaries, which may not reflect real-world conditions accurately. Therefore, for better convenience and accuracy in subsequent crack propagation study, it is more appropriate to use H8Z7H5 load distribution.

4.1.2. *Stress intensity factor*

To investigate the influence of initial crack length on the stress intensity factor, three kinds of initial crack length were considered: 5 mm, 10 mm, and 15 mm. The results of stress intensity factor and cracking angle were shown in Fig. 9(a)~Fig. 9(d), respectively. The distances shown are from the left edge of the model (along the y-axis). The upper x-axis indicates the locations of the wheel load prints. The three red dashed lines represent the position of three horizontal seams.

It is evident that the length of the initial cracks significantly affects the cracking behavior. Generally, cracks located closer to the center of the model horizontally have a greater impact on the stress intensity factor at the crack tip. For crack lengths ranging from 5 mm to 15 mm, shorter cracks tend to show higher maximum values for the stress intensity factors. Under static loading, the stress factor strength K_I is primarily influenced by the load position, with a less significant relationship to the transverse joint. K_I is almost always negative at different crack tip locations, indicating that cracks tend not to propagate under static loading; instead, they may even to closase, suggesting limited expansion of Type I cracks.

Similarly, the stress intensity factor K_{II} is negative at various crack tip locations and is mainly affected by the load position. However, where the load and joint overlap, there is a superposition effect that causes K_{II} to be larger than that at other locations. Positive and negative values of K_{II} reflect different expansion directions, indicating that shear cracks still have the tendency to expand.

The stress intensity factor K_{III} varies between positive and negative

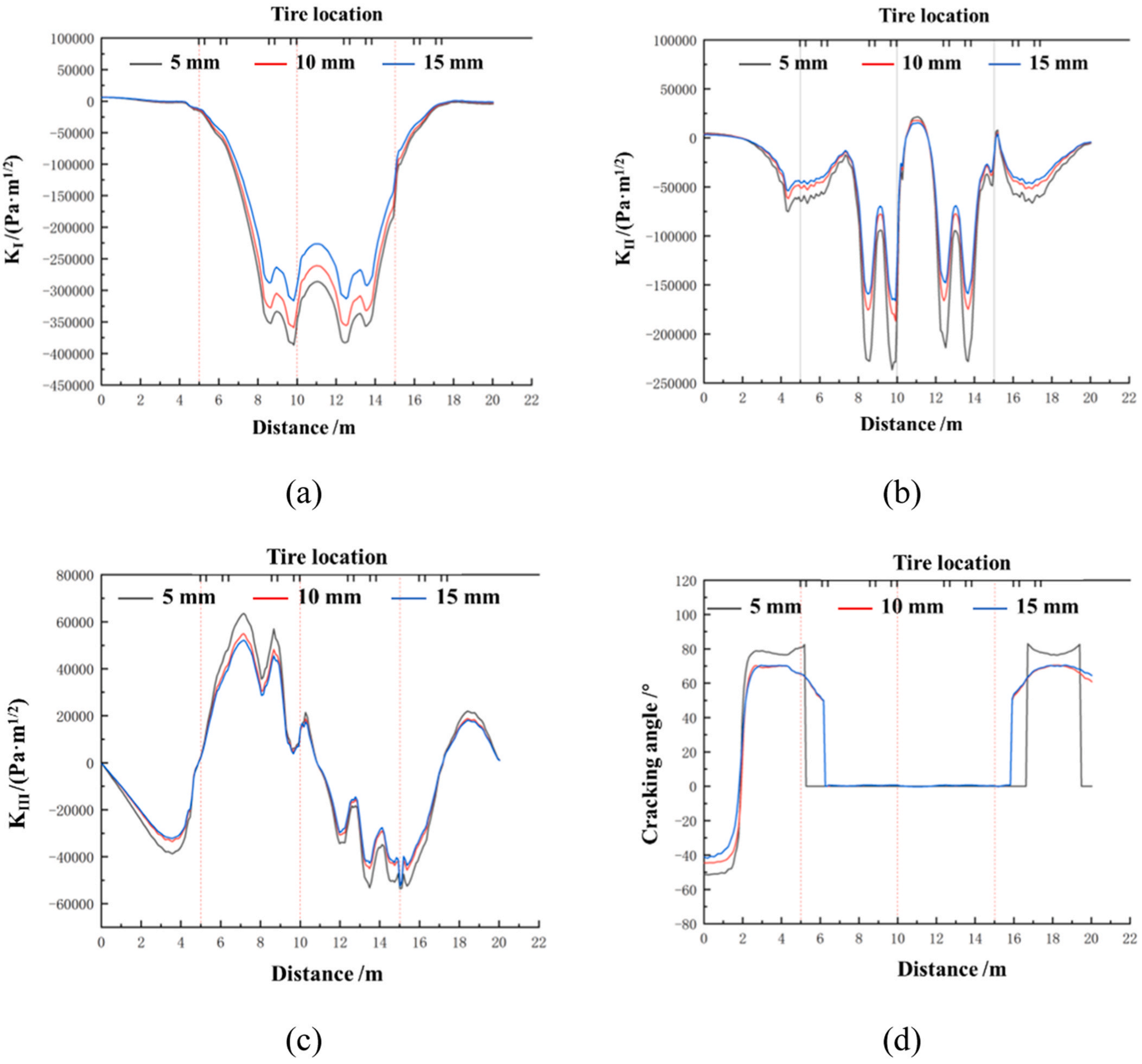

(a)

(b)

(c)

(d)

Fig. 9. Stress intensity factors and cracking angle under the action of critical static load (a) K_I, (b) K_{II}, (c) K_{III}, and (d) cracking angle.

values on distance, with the highest value occurring where the wheel prints are located. Although K_{III} affects the direction of crack expansion, its maximum value is considered smaller than that of K_{II}, suggesting that type III cracks are less prominent under static loads.

Regarding the cracking angle, its distribution on both sides of the model under static load is roughly symmetrical. Near the edges of the model, the cracking angle becomes more negative, while closer to the transverse joint, the angle becomes more positive. In the central region of the model between the transverse joints, the cracking angle is minimal. This distribution implied that cracks will expand vertically upward in the center of the model and diagonally at the edges. In summary, for cement concrete airport runways with asphalt overlays, the primary cracking mode under static load is type II cracks. Type III tearing cracks are less likely to occur, and Type I tension cracks are rare, consistent with previous studies [56].

4.2. *Cracking features under temperature-load coupling factors*

4.2.1. *Comparison of different analysis method*

Due to the long-term effect of temperature loads, repeated applying daily temperature variation in ABAQUS would require substantial computational time. Additionally, using XFEM in ABAQUS can lead to serious convergence problems. Therefore, this section explores two methods to address the convergence issue in cracking simulations under cyclic temperature loading: the traditional direct cyclic analysis step and the new Fatigue analysis step. The advantages and disadvantages of these methods are compared to determine the most suitable approach for subsequent temperature-load coupling analysis.

For the comparison, the initial crack length was set to 5 mm. To enhance the analysis efficiency, only the 15-hour cooling period from approximately 1 PM to 4 AM the next morning was used for direct cyclic simulation analysis. In this analysis, the single cycle time of t was set to 15 hours; the total number of cycles was set to 140,000; the maximum Fourier series order n was 25; and the maximum incremental step was

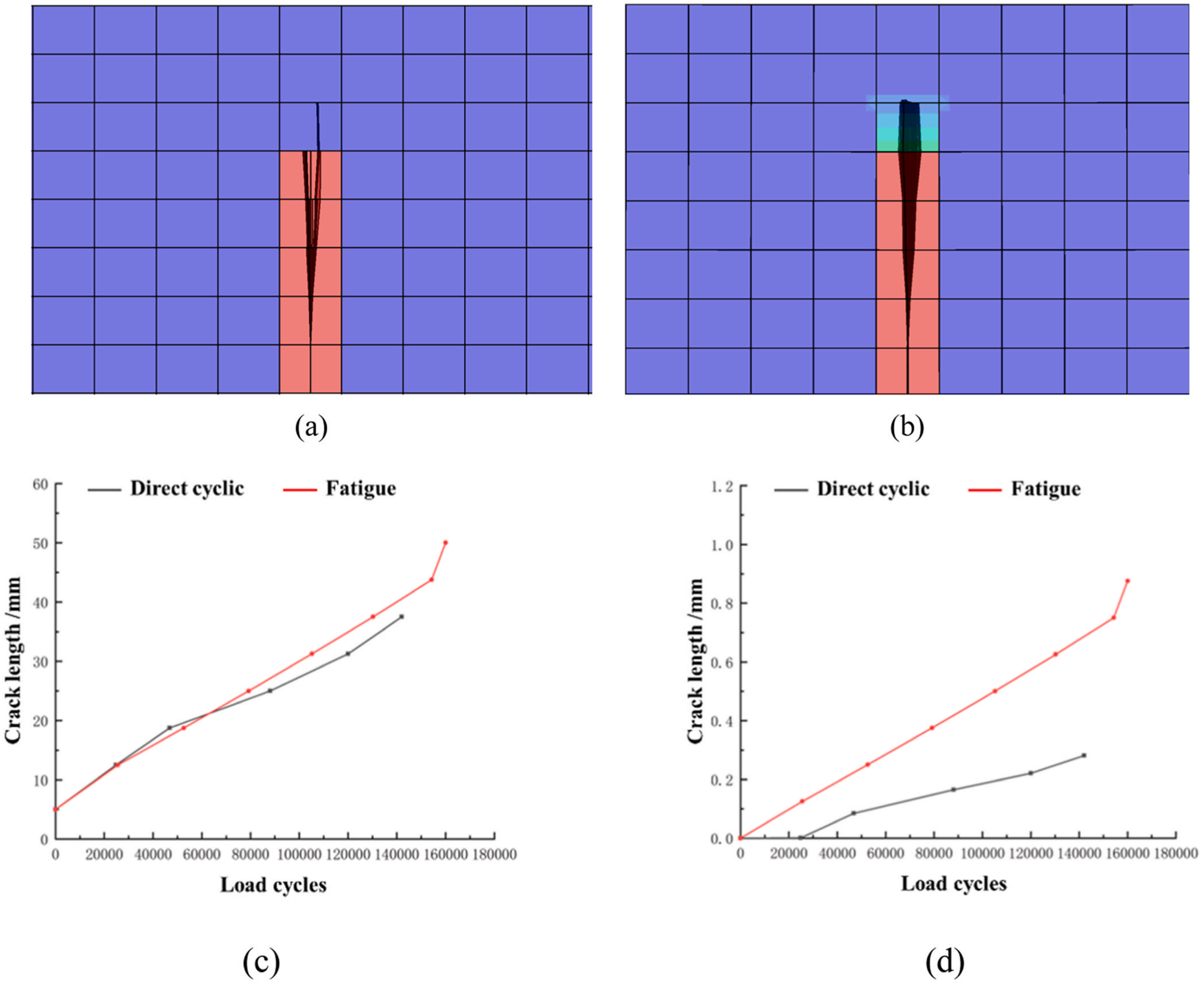

Fig. 10. Comparison of direct cyclic step and fatigue step (a) crack path of direct cyclic step, (b) crack path of fatigue step, (c) crack length of direct cyclic step, and (d) crack length of fatigue step.

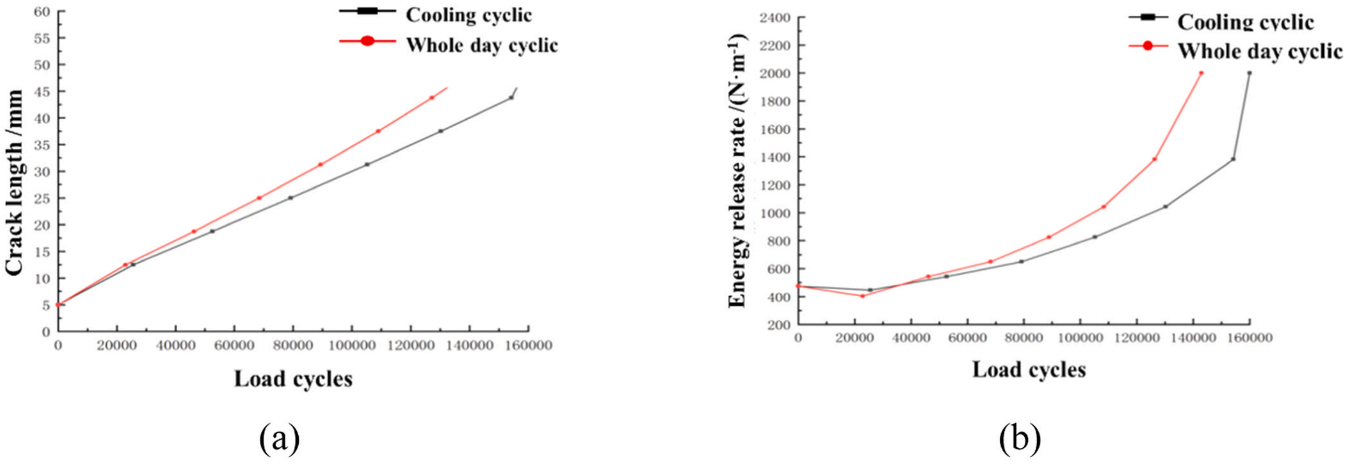

Fig. 11. Comparison between cracking features under the action of cooling cyclic and whole day's temperature range through (a) crack length, and (b) energy release rate.

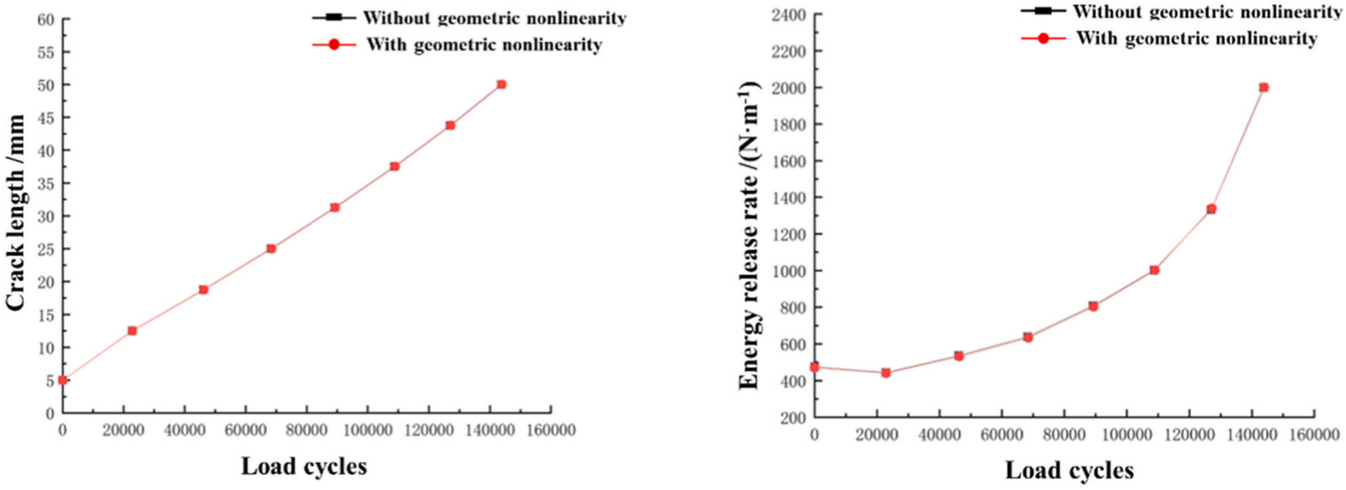

(a)

(b)

Fig. 12. Comparison between calculation results with and without geometric nonlinearity through (a) crack length, and (b) energy release rate.

set to 0.25 hours, based on the requirements of being less than *t/(2 n+1)*. For the Fatigue step settings, to ensure complete crack penetration, the number of cycles was increased to 160,000, with a cycle increment set to 0.02 hours, and the damage tolerance was left at default value of ABAQUS. The crack propagation paths and result data from both analysis methods are shown in Fig. 10(a)~Fig. 10(d), respectively, where crack length is as the vertical distance in the Z-axis direction.

By comparing the four images from Fig. 10(a)~Fig. 10(d), it is evident that when the model size, calculation parameters, mesh scheme, and temperature cyclic are identical, the from both analysis methods are similar in terms of crack length, particularly when the load cycles are relatively few. However, as the number of load cycles increases, the fatigue analysis method shows a higher crack propagation rate compared to the direct cyclic method.

The crack location and length can be easily monitored by examining the cracked regions in Fig. 10(a) and Fig. 10(b). Nonetheless there are notable differences between the two methods, particularly regarding calculation time and geometric nonlinearity. The direct cyclic method requires over 30 hours of computation and does not accommodate geometric nonlinearity, leading to poor convergence. In contrast, the Fatigue analysis method takes less than 10 hours and supports geometric nonlinearity, resulting in better convergence. Additionally, according to ABAQUS user's manual, the Fatigue step is better suited for calculating the mechanical response of thermosetting materials like asphalt concrete. Consequently, the Fatigue step was chosen for further analysis.

4.2.2. *Crack evolution at fatigue conditions*

Based on the aforementioned advantages, the Fatigue step is suitable for analyzing the mechanical response of the structure under the influence of a full day's temperature variation. Additionally, incorporating geometric nonlinearity enhances the accuracy of crack calculations. For a clearer understanding, Fig. 11(a) and Fig. 11(b) compare the cracking features under cooling cyclic conditions with those under the full day' temperature range, while Fig. 12(a) and Fig. 12(b) compares calculations with geometric nonlinearity to those without it.

From Fig. 12(a) and Fig. 12(b), it is evident that both the cracking speed and energy release rate are higher under the full day's temperature ranged compared to the cooling cyclic conditions. When the crack completely penetrates the asphalt overlay, the cooling cyclic requires 11331 more cycles than the full day's cyclic analysis with a delay of 7.93 %. Additionally, the energy release rate during the steady cracking period is 3.9 % lower for the cooling cyclic analysis compared to the full day's cyclic analysis. These results suggests that using cooling cyclic conditions to analyze the cracking behavior of asphalt overlay has a negligible impact on calculation accuracy. The fatigue step, therefore, enables efficient and accurate analysis of reflective crack in asphalt overlay.

Table 3
Working conditions for comparing cracking behavior with different overlay type, vertical crack location and load type.

Group name	EA1	EA2	EA3	SMA
Material	EAM	EAM	EAM	SMA−13
Location	Bottom of overlay	Top of overlay	Bottom of overlay	Bottom of overlay
Load type	Temperature-load coupling	Temperature-load coupling	Temperature only	Temperature-load coupling

Having determined the calculation method for analyzing reflective cracks in asphalt overlay, the next step is to investigate the influence of various factors on cracking behavior. Four aspects will be examined: load conditions, initial crack length and horizontal location, linear shrinkage coefficient, and asphalt overlay thickness. These factors will be detailed in the following sections.

4.2.3. *Comparison of crack propagation with different asphalt overlay*

To analyze the differences between temperature-only action and temperature-load coupling action, as well as the effects of vertical crack location and different asphalt overlay materials, four working conditions were investigated separately, as shown in Table 3. Two types of materials were considered: epoxy asphalt mixture (EAM) and SMA-13. The material parameters were referred from [51] and [27], respectively.

During the analysis, the model incorporated the whole-day temperature variation and utilize the fatigue. The maximum number of load cycles was set to 200000. The simulation results are presented in Fig. 13(a)~Fig. 13(d).

It can be seen from Fig. 13(a)~Fig. 13(d) that the cracking behaviors under temperature-load coupling and temperature-only conditions are relatively the same, indicating that, during long-term service, aircraft load has limited impact on crack propagation in asphalt overlays. This is because the energy release rates for temperature-load coupling and temperature-only conditions predominately involve Type I cracks, which are driven by tensile stress. Additionally, static analysis results show that the loading effect mainly influences Type II shear cracks, with

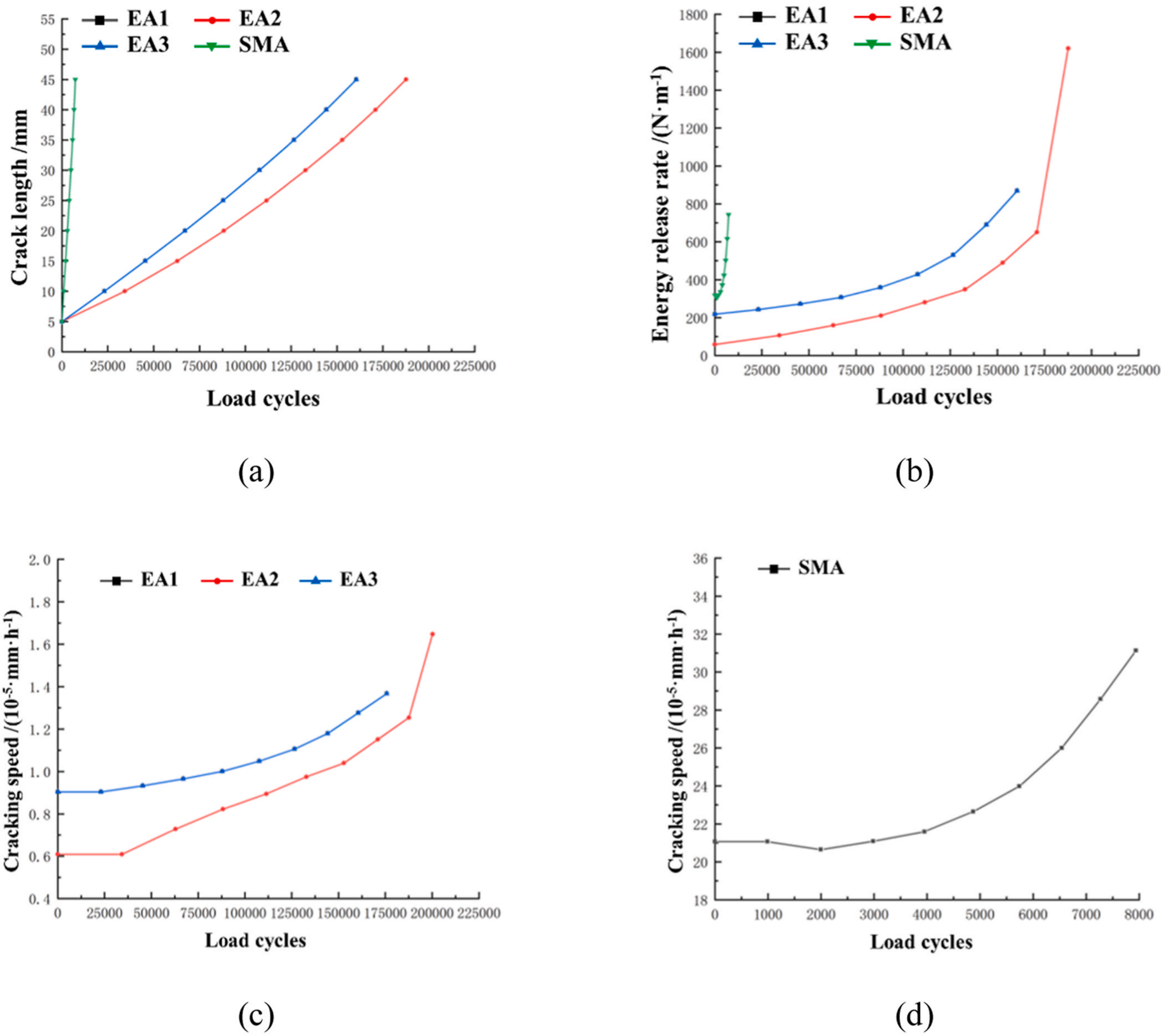

(a)

(b)

(c)

(d)

Fig. 13. Cracking behavior under different load conditions through (a) crack length, (b) energy release rate, and (c) and (d) cracking speed.

a smaller impact on Type I cracks. On the other hand, applying the aircraft load only 1500 times at 24-hour intervals in the calculation process, while more reflective of real-world conditions, results in negligible fatigue accumulation due to the spase loading frequency compared to the temperature effects.

Regarding overlay materials, it is evident that the fatigue life of the EAM is significantly greater than that of SMA-13. For the same crack extension length, SMA-13 exhibits a much higher cracking rate—over 10 times that of EAM. Although the difference in energy release rate between SMA-13 and EAM is not substantial (within 1000 N/m), SMA-13's lower fracture energy (900 N/m) contributes to its faster cracking. According to ABAQUS default settings, if the energy release rate ΔG exceeds 0.85 times the fracture energy, to the crack progresses to destabilization. Thus, despite similar energy release rates, SMA-13 cracks develop more rapidly until destabilization occurs. Using the Paris formula, the initial cracking speed of SMA-13 was found to be more than 10 times greater than that of EAM, confirming the reliability of the crack propagation comparison results.

Regarding the vertical position of the initial crack, reflective cracks at the bottom of the EAM expanded faster than top-down normal temperature-shrinkage cracks. The initial energy release rate for reflection cracks was 3.7 times higher than for normal temperature-shrinkage cracks. The reflective crack began expanding 110000 loading cycles earlier and fully penetrated 587000 cycles earlier that the normal crack. Additionally, the maximum crack expansion rate during stabilization was 10 % faster for reflective cracks compared to normal crack. While reflective cracks expand faster, the difference is not several times greater. Furthermore, it has been observed that micro-cracks are more-likely to occur on the surface of asphalt pavement under heavy aircraft loads, suggesting that the upper layer may be more susceptible to initial cracking that the lower layer, and both upper and lower cracks may expand simultaneously through the asphalt pavement.

4.2.4. Influence of crack length and horizontal location

The previous section discussed the cracking behavior of an initial crack located directly at the center of joint with a length of 5 mm. To investigate cracking behavior in more detail, three initial crack lengths – 5 mm, 10 mm, and 15 mm – were analyzed, and the results are shown in Fig. 14(a)~Fig. 14(c). Regarding the horizontal location of the initial crack, four conditions were considered: cracks 10 mm and 5 mm from

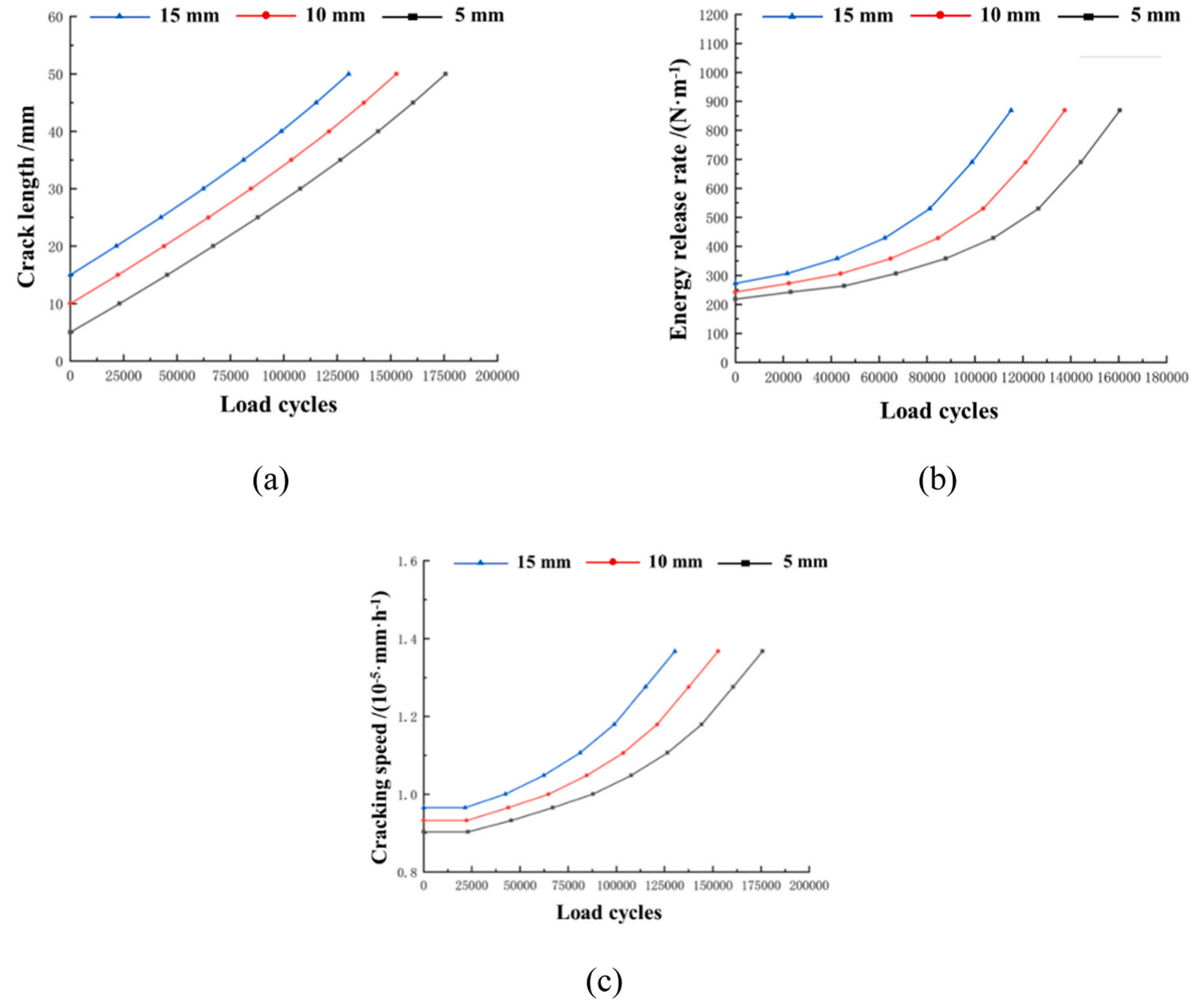

(a)

(b)

(c)

Fig. 14. Influence of initial crack length on (a) crack length, (b) energy release rate, and (c) cracking speed.

the center panning along the positive direction of the x-axis (groups DIS1 and DIS2, respectively), cracks 10 mm and 5 mm from the center, panning along the negative direction of the x-axis (groups DIS4 and DIS3, respectively). The cracking paths for these conditions are illustrated in Fig. 15(a)~Fig. 15(d), while a comparison of cracking-related parameters is shown in Fig. 16(a)~Fig. 16(c). The values for the control subject, which involves the initial crack located on the center of the joint, are also provided for reference.

It can be concluded that the longer the initial crack length, the greater the degree of crack extension for the same number of loading cycles. However, when the three crack lengths are equal, the extension behavior is very similar. This is due to the tensile stress-dominated nature of Type I cracks under variable temperature conditions, causing all cracks to extend almost vertically within minimal horizontal displacement. As a result, the initial conditions of the three different crack lengths are effectively equivalent to different degrees of the same crack. Furthermore, the variations in energy release rate and cracking speed during crack extension for the three initial crack lengths are also very similar. The number of load cycles at the coordinate points in the figure corresponds to the crack lengths at each stage. By comparing the energy release rate and cracking speed across different plots, it is evident that the energy release rates and cracking speeds for the three groups of cracks with the same crack lengths are nearly identical.

Analyzing Fig. 15(a)~Fig. 15(d) and Fig. 16(a)~Fig. 16(c) reveals that reflective cracks near the central transverse joint of the cement slab tend to move closer to the vertical plane directly aligned with the transverse joint. Additionally, the closer a reflective crack is to the center, the greater the degree of vertical expansion for the same number of load cycles. The horizontal offset of left-right symmetric directions has minimal impact on the extent of crack expansion, with both symmetrically distributed cracks exhibiting almost identical expansion for the same number of load cycles. There is only a small difference in the degree of crack extension between cracks offset by 5 mm and those directly centered on the reflective crack. However, a more significant difference is observed in the degree of crack extension between cracks offset by 10 mm and those offset by 5 mm or centered.

Regarding the energy release rate, cracks closer to the transverse joint exhibit higher energy release rates, and this difference increases as the number of load cycles grows. Among the symmetrically distributed cracks, the energy release rates for the two groups within a 5 mm offset are almost identical, with a maximum energy release rate of about 519.9 N/m during the stable expansion phase, which is 40.7 % lower than that of the central crack. Similarly, the energy release rates for the two groups of cracks with a 10 mm offset are nearly identical, showing

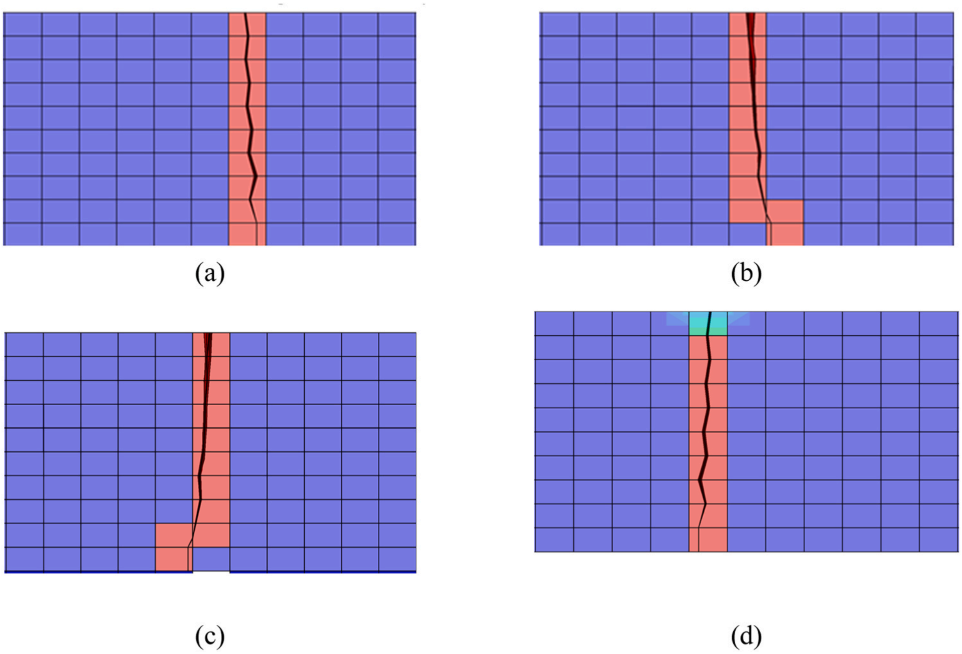

Fig. 15. Schematic of cracking path for (a) group DIS1, (b) group DIS2, (c) group DIS3, and (d) group DIS4.

only minor differences during the initial expansion phase. The maximum energy release rate for the 10 mm offset cracks is approximately 515.3 N/m, which is 40.2 % lower than that of the central crack. Unlike the steady increase in the energy release rate observed for the central crack during the stable expansion phase, the energy release rate for offset cracks fluctuates significantly in the early stages. This fluctuation may be due to variations in crack paths. Initially, the energy release rate of the crack with a 5 mm offset is lower than that of the10 mm offset but eventually surpasses it and remains higher throughout the expansion.

4.2.5. *Influence of linear shrinkage coefficient*

The linear shrinkage coefficient determines the average elongation or shrinkage of the material during heating or cooling, which affects the deformation behavior of each layer of the runway. In the model, the deformation of the asphalt overlay in a variable temperature environment is constrained not only by the boundary conditions, which generate temperature-induced stress, but also by the relative constraints imposed by the cement concrete layer, due to the difference in line shrinkage coefficients between the asphalt overlay and the cement concrete layer. This effect is particularly pronounced at the joints of cement slabs, where the overlay is subjected to the more significant tensile and shear stresses. Using an asphalt overlay shrinkage coefficient of 2.6×10^{-5} as the control reference, shrinkage coefficients of 1.74×10^{-5}, 2.03×10^{-5}, 2.31×10^{-5}, and 3.00×10^{-5}- designated as LSC1, LSC2, LSC3, and LSC4, respectively – were investigated in detail. The initial crack length was set to 5 mm, and the calculation results are shown in Fig. 17(a)~Fig. 17(c).

The figure shows that the smaller the shrinkage coefficient, the more difficult it is for the crack to propagate. For the same number of load cycles, a smaller shrinkage coefficient results in a shorter crack length and a lower the energy release rate. When the crack extension reaches the stabilization stage, compared to the LSC1 group (with the smallest shrinkage coefficient), the maximum energy release rates of the other four groups with increasing coefficients of shrinkage are 14.3 %, 29.0 %, 45.1 %, and 68.9 % higher, respectively, than those of the LSC1 group. The LSC4 group, which has the largest shrinkage coefficient, shows a dramatic increase in energy release rate and exhibits obvious instability in the later stages of crack extension. This is because, under these conditions, when the load cycles increase from 137,500 to 150,000, the initial crack has penetrated the entire asphalt overlay. However, the exact cycle count at which penetration occurs is not identifiable during the process, leading to an extremely high energy release rate at the 150,000-cycle mark. Similarly, the larger the shrinkage coefficient, the faster the cracking speed for the same number of load cycles, with the greatest difference in cracking speed – up to 7.2 % – observed between the LSC1 and LSC4 groups. In the stable expansion stage, the maximum cracking speeds for the LS2, LS3 and control groups are 4.1 %, 7.9 % and 11.8 % faster, respectively, than those of the LSC1 group. Considering that the original cement concrete runway has a shrinkage coefficient of 1.2×10^{-5}, it is evident that when the shrinkage coefficient of the asphalt overlay is smaller (closer to that of the cement concrete runway), the relative temperature-induced shrinkage deformation between the two becomes smaller. This reduces the tensile effect of the cement concrete slab on the thermosetting modified asphalt paving overlays, making crack propagation more difficult. These findings indicate that reducing the shrinkage coefficient of asphalt overlay can help decrease stress concentration in the overlay, thereby improving the fatigue performance of paving or cover layer, and effectively slowing down the expansion of reflective cracks.

4.2.6. *Influence of the thickness of asphalt overlay*

Typically, increasing the thickness of an asphalt overlay can effectively inhibit the propagation of reflective cracks in pavement engineering. However, research on the feasibility of this method for airport runway overlays is limited. In China, the recommended thickness for asphalt overlays on airport runways is between 5 cm and 8 cm. Therefore, this study investigated the cracking behavior for overlay thickness of 5 cm, 7 cm, and 9 cm, respectively. To ensure complete penetration of the overlay, the total number of load cycles were set at 250000. The simulation results are shown in Fig. 18(a)~Fig. 18(c).

It is apparent that increasing the thickness of asphalt overlay can effectively delay the initial crack propagation and finial penetration times. When the thickness of the asphalt overlay is increased from 5 cm to 7 cm, the initial propagation is delayed by 8812 load cycles. This delay further increases to 24853 load cycles when the thickness reaches 9 cm. Similarly, the total penetration time is delayed 67008 cycles when the thickness is increased to 7 cm, and complete penetration is not

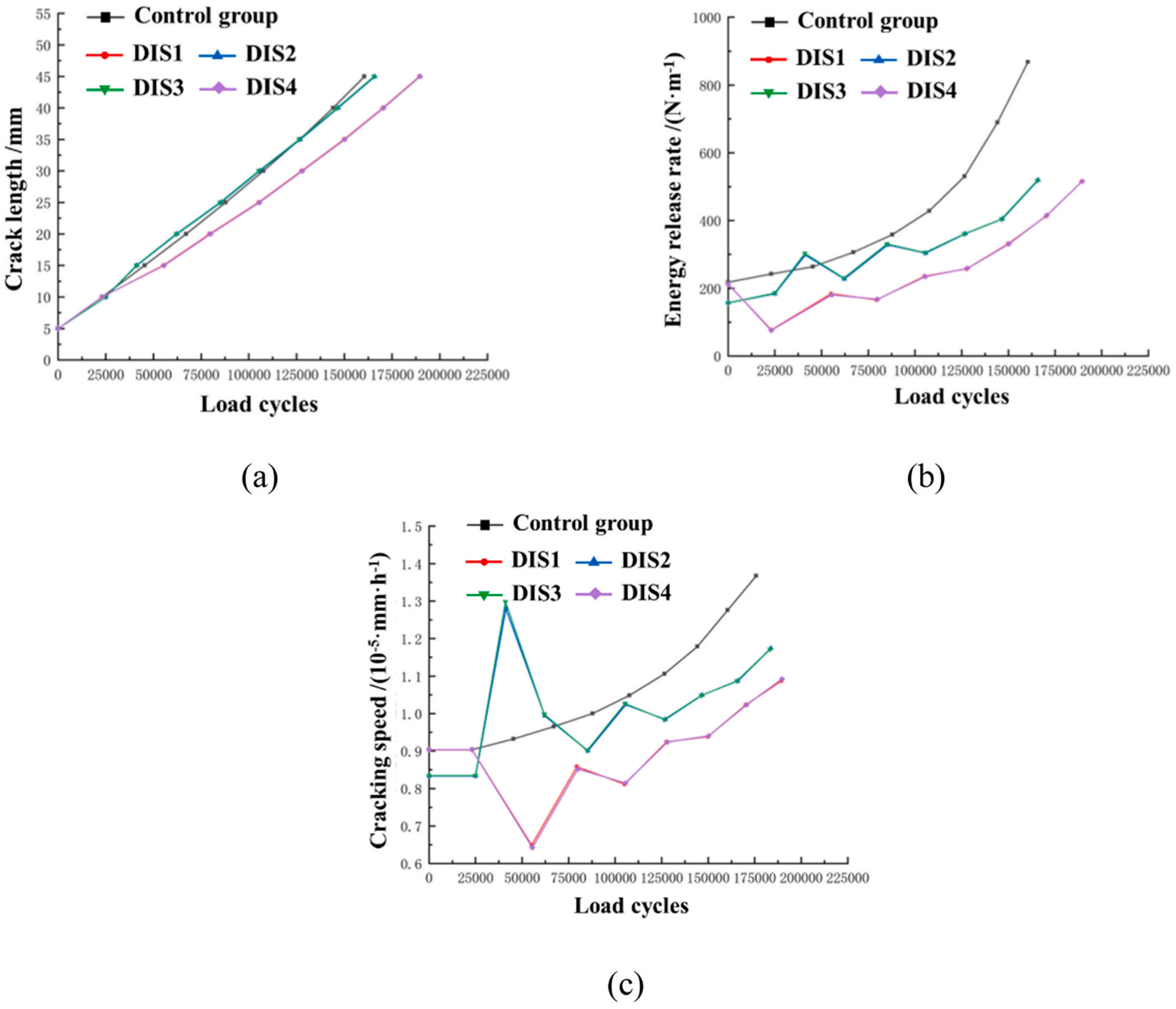

Fig. 16. Influence of the horizontal location of initial crack on (a) crack length, (b) energy release rate, and (c) cracking speed.

achieved when the thickness is 9 cm. Furthermore, a greater overlay thickness results in a lower the energy release rate and slower cracking speed. When the overlay thickness increases from 5 cm to 7 cm, the energy release rate decreases by 19.1 %; this decrease becomes 52.3 % when the thickness increases from 7 cm to 9 cm. This indicates that increasing the thickness of the asphalt overlay effectively prevents the propagation of reflective cracks.

Regarding cracking speed, the early crack expansion rates of 9 cm and 7 cm thick overlay are approximately 27.6 % and 51.9 % lower, respectively, than that of 5 cm thick overlay. The increase in crack expansion rate for the 5 cm thick overlay is about 51 %, while for the 7 cm thick overlay, it is approximately 49.3 % during the temperature-load coupled cycling. The maximum crack expansion rate is only 13.1 % for 9 cm thick overlay, which does not completely penetrate within the finite number of cycles. In summary, increasing the thickness of the asphalt overlay is an effective way to prevent the propagation of reflective cracks, which can be attributed to the significant reduction of energy release rate and cracking speed.

5. Conclusions

This study focuses on the asphalt overlay of airport runway and investigates the cracking behavior of the overlay in detail using the XFEM in detail. An XFEM model was firstly established in ABAQUS to analyze the critical load position under static aircraft load. Then, the cracking behavior under temperature-load coupling factors was studied using this model. To quantitatively analyze the anti-cracking performance of the asphalt overlay, the optimal analysis method was identified, and the cracking process was examined in detail. Finally, different factors influencing the cracking behavior were discussed thoroughly. The workflow established in this study can be applied to analyze the cracking characteristics of similar structures. Additionally, the results provide a reference for engineering practices involving the application of epoxy asphalt mixture (EAM) in asphalt overlays. The main findings and conclusions are as follows:

- Horizontal tensile and shear stresses on the airport asphalt overlay, particularly in the areas above the transverse joints at the edges of the old cement slabs during the rough landing dynamic loading, are the primary cause of the reflective cracks. Specifically, the maximum

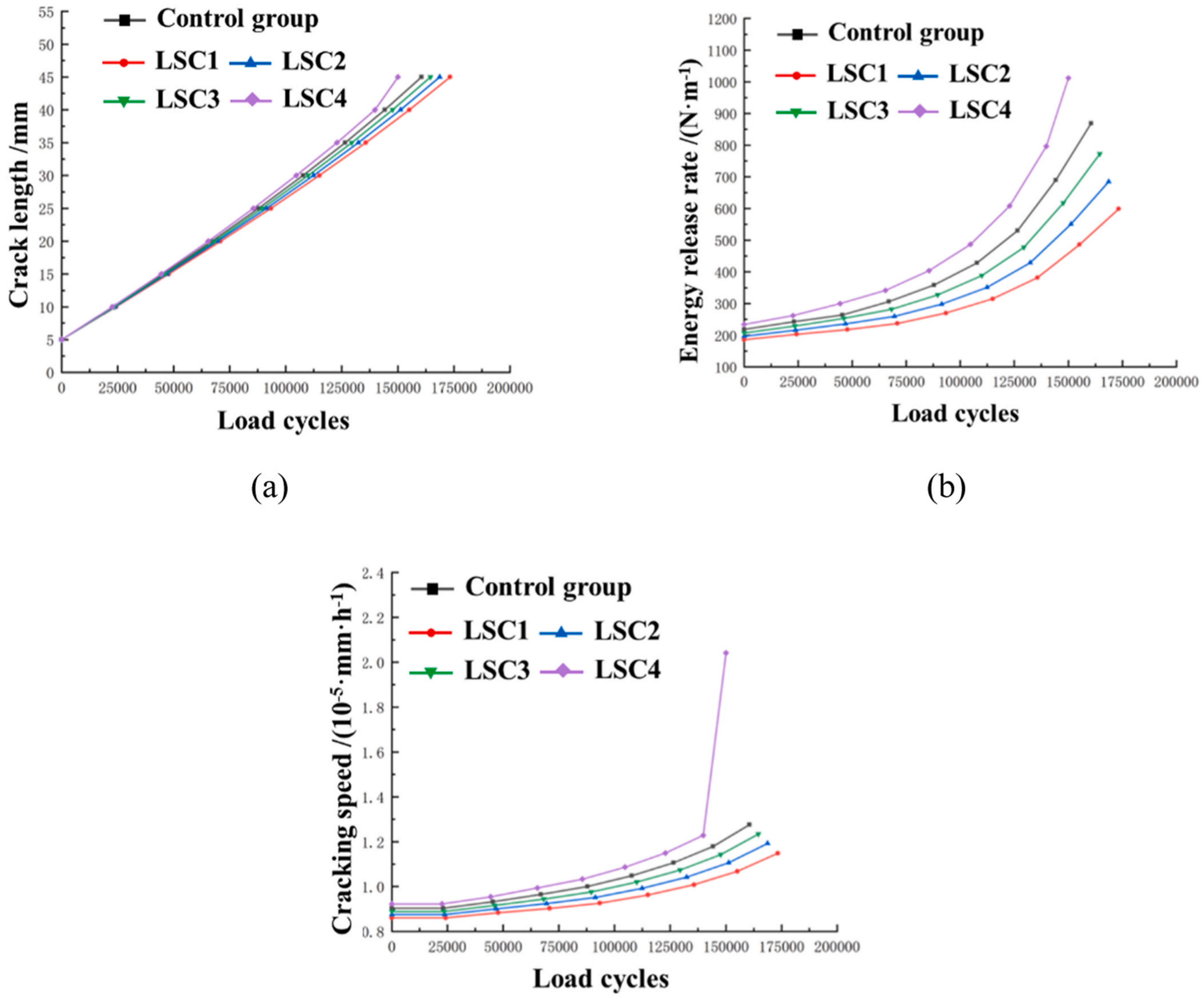

(a)

(b)

(c)

Fig. 17. Influence of the shrinkage coefficient on (a) crack length, (b) energy release rate, and (c) cracking speed.

shear stress S_{13} observed under the most critical loading condition, H8Z7H5, was 1.59×10^{6} Pa. This observation is consistent with cracking behavior observed in various asphalt applications, highlighting the need for precise stress management in overlay design.

- The vertical compressive stress concentration at the top of the asphalt overlay layer is closely related to the aircraft's loading position. In contrast, the horizontal tensile stress concentration at the bottom of the layer and the horizontal shear stress concentration at the bottom are more influenced by the position of the joints in the old cement concrete runway. For example, under static load conditions, the maximum stress intensity factor K_{II} was found to be larger than K_{I}, indicating shear cracks are more likely to propagate. The stress intensity factor K_{II} reached up to -1.33×10^{6} Pa for crack tip locations.
- The expansion of reflective cracks in the airport runway asphalt overlay under temperature variation is more effectively and efficiently modelled using Fatigue cyclic analysis. Specifically, the fatigue analysis step only takes less than 10 hours when doing the whole calculation, whose value is only 1/3 of direct cyclic analysis step The fatigue analysis results showed that the cracking speed under full-day temperature variations was 7.93 % faster than under cooling cyclic conditions. Energy release rates were also 3.9 % higher under the full-day scenario. The accelerated crack propagation under full-day temperature cycles demonstrates the universal importance of considering thermal effects when designing and maintaining pavements, especially in regions prone to extreme or fluctuating temperatures.
- Under aircraft loading, the primary model of crack expansion is the Type II shear crack, with Type I open crack and Type III tearing crack being less likely. The crack expansion angle results indicate a tendency for cracks to propagate vertically upward at the center of the model and at an angle near the model's edge.
- Initial cracks at the bottom of the asphalt overlay are unlikely to reach the upper surface of the layer when only vertical aircraft load is considered. Initial cracks of 5 mm do not significantly expand by the end of the cycle; 10 mm initial cracks extend horizontally but not significantly vertically; and 15 mm initial cracks extend upward towards the top of the layer but still spread out in all directions.
- Reducing the asphalt shrinkage coefficient significantly improves the cracking performance of the overlay, effectively slowing the

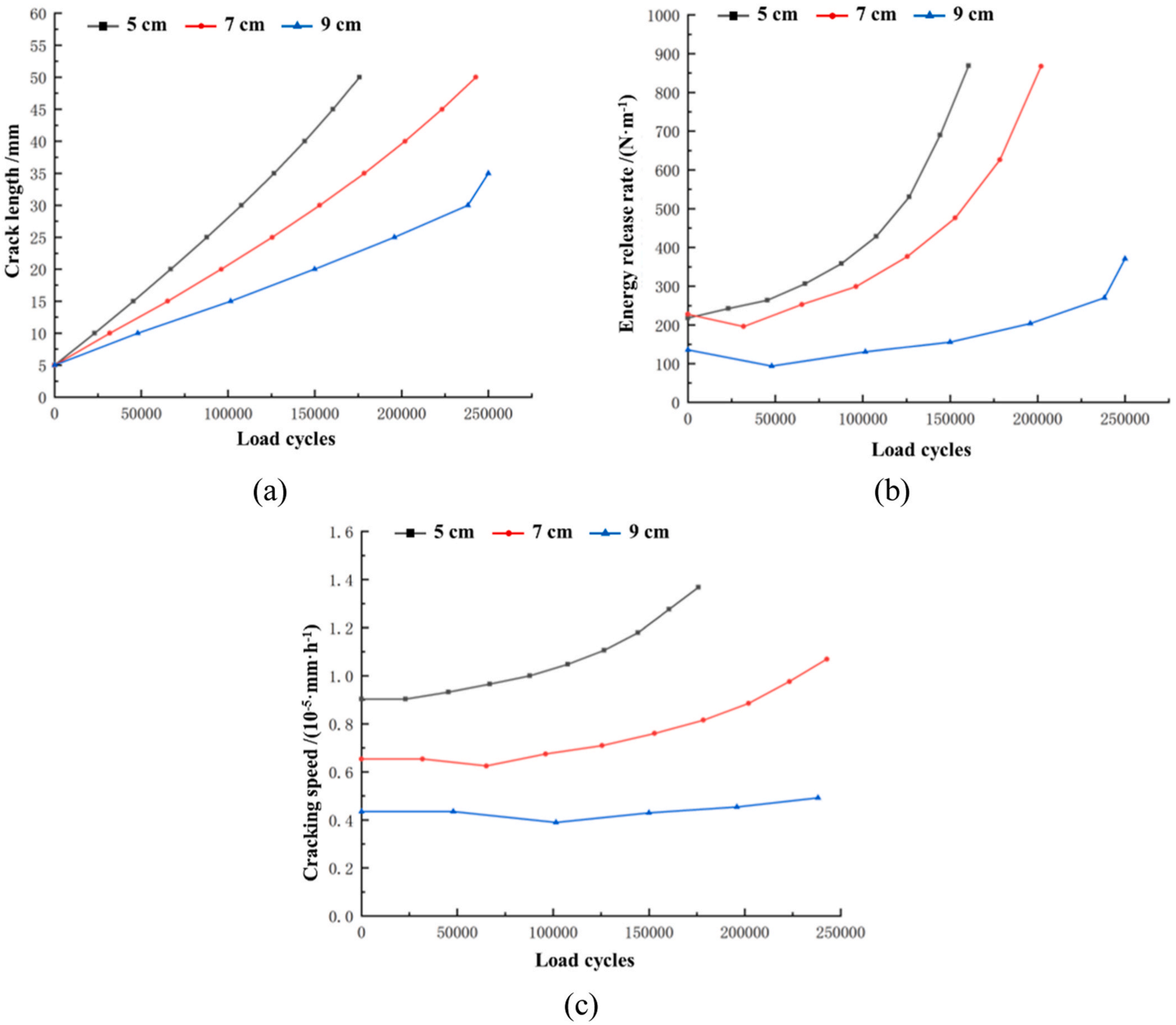

Fig. 18. Influence of the overlay thickness on (a) crack length, (b) energy release rate, and (c) cracking speed.

propagation speed of reflection cracks. Increasing the thickness of the overlay not only delays the total time for reflective crack expansion but also reduces the cracking speed and the energy release rate during the steady crack growth stage. For instance, increasing the overlay thickness from 5 cm to 7 cm delayed total crack penetration by 67,008 cycles. Similarly, the energy release rate for a 9 cm overlay was 52.3 % lower than for a 5 cm overlay during steady crack growth. his is critical for improving the long-term durability of pavements across diverse environmental and loading conditions.

However, this study only focuses on the temperature variation in a single day and doesn't consider seasonal temperature variations, especially in cold regions where temperatures can drop rapidly over a short period. Additionally, tilted initial cracks, which are common in engineering practice, were not considered in this study. Moreover, calibration between the simulation results and in-situ test data is necessary to improve the model's reliability. Further research should aim to develop more accurate temperature fields, consider more practicable working conditions, and validate the results across various scenarios.

CRediT authorship contribution statement

Long Sun: Writing – original draft, Visualization, Investigation, Formal analysis. **Chong Zhan:** Writing – original draft, Investigation, Data curation. **Ruochong Yang:** Writing – review & editing, Writing – original draft, Supervision, Methodology, Conceptualization. **You Wu:** Writing – review & editing, Writing – original draft, Methodology. **Yulou Fan:** Visualization, Data curation. **Hongbo Liu:** Supervision, Resources. **Jun Yang:** Writing – review & editing, Supervision, Resources, Funding acquisition. **Chenguang Shi:** Writing – review & editing, Methodology.

Declaration of Competing Interest

The authors declare that they have no known competing financial interests or personal relationships that could have appeared to influence the work reported in this paper.

Acknowledgment

The authors acknowledge the financial support of the National

Natural Science Foundation of China (No. 52378444, No. 52078130).

Data availability

Data will be made available on request.

References

[1] Report on transportation development in China, China Market Press2022.
[2] J.G. Speight, Chapter 8 – Uses of Asphalt, Asph. Mater. Sci. Technol. (2015) 341–359.
[3] N.S. Correia, T.R. Souza, M.P.S. Silva, V.V. Kumar, Investigations on interlayer shear strength characteristics of geosynthetic-reinforced asphalt overlay sections at Salvador International Airport, Road. Mater. Pavement Des. 24 (6) (2022) 1542–1558.
[4] A.A. Zaini, M.M. A. Aziz, K.A. Kassim, K.H. Mustafa, A review on crack relief layer in airport runway, J. Teknol. 78 (7-2) (2016).
[5] T. Rahman, B. Suhendro, H.C. Hardiyatmo, W. Sartono, P. Nawangalam, Airfield asphalt overlay design for non-conventional pavement structures: a case study of airport in Indonesia, J. Civ. Eng. Forum (2022) 125–138.
[6] O.Y. Bayraktar, Use of geosynthetics in road construction, Kast. Univ. J. Eng. Sci. 6 (2) (2020) 107–113.
[7] A.J. Puppala, A. Banerjee, S.S.C. Congress, Geosynthetics in geo-infrastructure applications, in: K.L. Reifsnider (Ed.), Durability of Composite Systems, 7, Woodhead Publishing, 2020, pp. 289–312.
[8] W.J. Robinson, L. Howard Isaac, S. Tingle Jeb, J.Norwood Gregory, Analysis of full-scale geosynthetic reinforced airfield pavement subjected to accelerated aircraft loading, J. Transp. Eng., Part B: Pavements 146 (3) (2020) 04020052.
[9] E. Solatiyan, N. Bueche, A. Carter, Mechanical characterization of grid-reinforced interfaces within rehabilitated bituminous layers, Constr. Build. Mater. 288 (2021) 122989.
[10] S.A. Safavizadeh, S.-H. Cho, Y.R. Kim, Interface shear strength and shear fatigue resistance of fibreglass grid-reinforced asphalt concrete test specimens, Int. J. Pavement Eng. 23 (8) (2022) 2531–2542.
[11] A.B. Crusho, S. Niveditha, A state-of-art review on the interfacial bond strength of bituminous overlay in asphalt pavements, Int. Adv. J. Eng. Res. 3 (2020) 20–26.
[12] G. White, State of the art: asphalt for airport pavement surfacing, Int. J. Pavement Res. Technol. 11 (1) (2018) 77–98.
[13] I.I. Idris, H. Sadek, M. Hassan, State-of-the-art review of the evaluation of asphalt mixtures' resistance to reflective cracking in laboratory, J. Mater. Civ. Eng. 32 (9) (2020).
[14] S. Deilami, G. White, Review of reflective cracking in composite pavements, Int. J. Pavement Res. Technol. 13 (5) (2020) 524–535.
[15] X. Wang, K. Li, Y. Zhong, Q. Xu, C. Li, XFEM simulation of reflective crack in asphalt pavement structure under cyclic temperature, Constr. Build. Mater. 189 (2018) 1035–1044.
[16] H.Z. Wang, Y. Wu, J. Yang, H.P. Wang, Numerical simulation on reflective cracking behavior of asphalt pavement, Appl. Sci.-BASEL 11 (17) (2021).
[17] X. Wang, Y. Zhong, Reflective crack in semi-rigid base asphalt pavement under temperature-traffic coupled dynamics using XFEM, Constr. Build. Mater. 214 (2019) 280–289.
[18] H. Ziari, M.R.M. Aliha, E.S. Fard, M.J. Sarbijan, Mixed mode I+II fracture parameters and cracking trajectory of heterogeneous multilayer pavement structure containing reflective crack, Fatigue Fract. Eng. Mater. Struct. 45 (10) (2022) 2958–2977.
[19] J. Gallego, J.N. Prieto, New laboratory equipment for study of reflective cracking in asphalt overlays, Transp. Res. Rec. 1970 (1) (2006) 215–222.
[20] X. Wang, Y. Zhong, Influence of tack coat on reflective cracking propagation in semi-rigid base asphalt pavement, Eng. Fract. Mech. 213 (2019) 172–181.
[21] H. Ye, X. Wang, N. Fang, Z. Su, X. Sun, Interlayer working conditions classification and treatment measures of airport asphalt pavement overlay, J. Adv. Transp. 2019 (2019) 1–16.
[22] Z. Zhao, X. Guan, F. Xiao, Z. Xie, P. Xia, Q. Zhou, Applications of asphalt concrete overlay on Portland cement concrete pavement, Constr. Build. Mater. 264 (2020).
[23] C. Atkinson, R.V. Craster, Theoretical aspects of fracture mechanics, Prog. Aerosp. Sci. 31 (1) (1995) 1–83.
[24] M. Cervera, G.B. Barbat, M. Chiumenti, J.Y. Wu, A comparative review of XFEM, mixed FEM and phase-field models for quasi-brittle cracking, Arch. Comput. Methods Eng. 29 (2) (2022) 1009–1083.
[25] A.A. Eltahan, R.L. Lytton, Mechanistic-empirical approach for modeling reflection cracking, Transp. Res. Rec. 1730 (1) (2000) 132–138.
[26] H.D. Kuai, H.J. Lee, J.H. Lee, S. Mun, Fatigue crack propagation model of asphalt concrete based on viscoelastic fracture mechanics, Transp. Res. Rec. 2181 (1) (2010) 11–18.
[27] Z. Qian, F. Meng, J. Zeng, Airfield pavement with high performance asphalt concrete, J. Southeast Univ. (Nat. Sci. Ed.) (3) (2015) 575–580.
[28] P. Liu, X. Weng, G. Zhang, The load stress analysis of epoxy asphalt concrete overlay on airport composite pavement, Mater. Rev. 29 (20) (2015) 148–156.
[29] W. Ran, J. Ling, H. Zhao, Characteristics of epoxy asphalt pavement rutting based on accelerated pavement test, J. Build. Mater. 19 (2) (2016) 330–335.
[30] W. Ran, Y. Zou, E. Kong, Analysis of the SMA asphalt pavement rutting characteristics based on accelerated pavement testing, Highw. Eng. 41 (4) (2016) 6–11.
[31] G. Lefeuve-Mesgouez, D. Le HouÉDec, A.T. Peplow, Ground vibration in the vicinity of a high-speed moving harmonic strip load, J. Sound Vib. 231 (5) (2000) 1289–1309.
[32] Y. Wu, J. Xue, Y. Yu, C. Shi, Y. Fan, H. Wang, J. Yang, M. Gong, W. Huang, Research of reflective crack in asphalt pavement using SCB specimen and XFEM: from laboratory test to numerical simulation, Constr. Build. Mater. 406 (2023).
[33] H. Wang, Y. Wu, J. Yang, H. Wang, Numerical simulation on reflective cracking behavior of asphalt pavement, Appl. Sci. 11 (17) (2021).
[34] Y. Fan, Y. Wu, H. Chen, S. Liu, W. Huang, H. Wang, J. Yang, Performance evaluation and structure optimization of low-emission mixed epoxy asphalt pavement, Materials 15 (18) (2022).
[35] P. Xie, H. Wang, Finite element analysis of thermal-induced reflective cracking in composite pavement with mitigation strategies, Eng. Fract. Mech. 266 (2022) 108396.
[36] K.B. Broberg, Critical review of some theories in fracture mechanics, Int. J. Fract. Mech. 4 (1) (1968) 11–19.
[37] G.C. Sih, Elastodynamic crack problems, Springer Science & Business Media, 1977.
[38] S.Ahmad Kanth, A. Shafi Lone, G.A. Harmain, A. Jameel, Elasto Plastic Crack Growth by XFEM: A Review, Mater. Today.: Proc. 18 (2019) 3472–3481.
[39] I.M. Lancaster, H.A. Khalid, I.A. Kougioumtzoglou, Extended FEM modelling of crack propagation using the semi-circular bending test, Constr. Build. Mater. 48 (2013) 270–277.
[40] J. Zhang, D. Cao, J. Zhang, Three-dimensional modelling and analysis of fracture characteristics of overlaid asphalt pavement with initial crack under temperature and traffic loading, Constr. Build. Mater. 367 (2023).
[41] Y. Zhao, F. Ni, L. Zhou, Viscoelastic response of reflective cracking under dynamic vehicle loading in asphalt concrete pavements, ICCTP 2011: Towards Sustain. Transp. Syst. (2011) 3278–3297.
[42] J. Melenk, I. Babuska, Approximation with harmonic and generalized harmonic polynomials in the partition of unity method, Comput. Assist. Mech. Eng. Sci. 4 (1997) 607–632.
[43] J.M. Melenk, I. Babuška, The partition of unity finite element method: Basic theory and applications, Comput. Methods Appl. Mech. Eng. 139 (1) (1996) 289–314.
[44] K. Rege, H.G. Lemu, A review of fatigue crack propagation modelling techniques using FEM and XFEM, IOP Conf. Ser.: Mater. Sci. Eng. 276 (1) (2017) 012027.
[45] H. Fu, X. Liang, K. Chen, Y. Wang, Z. Xiao, Study on key mechanical properties of the flexible spoke non-pneumatic tire considering thermo-mechanical coupling, Adv. Eng. Softw. 173 (2022).
[46] W.H. BARBER, The genesis of voltaire's micromégas, Fr. Stud. XI (1) (1957) 1–15.
[47] Z. Yan, Analysis of the temperature field in layered pavement system, J. Tongji Univ. 3 (1) (1984) 76–84.
[48] R. Ghafoori Ahangar, Y. Verreman, Assessment of mode I and mode II stress intensity factors obtained by displacement extrapolation and interaction integral methods, J. Fail. Anal. Prev. 19 (1) (2019) 85–97.
[49] J. Chen, H. Wang, P. Xie, Pavement temperature prediction: theoretical models and critical affecting factors, Appl. Therm. Eng. 158 (2019) 113755.
[50] Y. Fan, Y. Yu, C. Shi, Y. Wu, S. Huang, Y. Zhou, H. Wang, J. Yang, W. Huang, Failure modes of asphalt pavement with top-down cracks based on measured aging gradients in field cores, Constr. Build. Mater. 438 (2024).
[51] Y. Fan, H. Chen, X. Yi, G. Xu, X. Cai, Y. Zhou, S. Huang, Y. Wu, H. Wang, J. Yang, W. Huang, Cracking resistance evaluation of epoxy asphalt mixtures with 100% reclaimed asphalt pavement (RAP), Constr. Build. Mater. 395 (2023).
[52] G. Xu, J. Zhou, X. Chen, Y. Liang, D. Cai, L. Lou, Temperature features of the asphalt concrete waterproofing layer on high-speed railway in cold regions, Constr. Build. Mater. 305 (2021).
[53] A. Alroqi, W. Wang, Comparison of aircraft tire wear with initial wheel rotational speed, Int. J. Aviat., Aeronaut., Aerosp. 2 (2015).
[54] K. Liu, Z. Wu, J. Yang, H. Guan, Study of dynamic response and fatigue damage of high-speed railway tunnels under the impact load of aircraft landing, Mod. Tunn. Technol. 59 (2) (2022) 96–102.
[55] C.H. Villanueva, K. Maute, Density and level set-XFEM schemes for topology optimization of 3-D structures, Comput. Mech. 54 (1) (2014) 133–150.
[56] J. Baek, Modeling reflective cracking development in hot-mix asphalt overlays and quantification of control techniques, 2010.